



Dynamic evaluation of a scaled-down heat pipe-cooled system during start-up/shut-down processes using a hardware-in-the-loop test approach

Jiao-Long Deng¹ · Tian-Shi Wang¹ · En-Ping Zhu¹ · Shuo Yuan¹ · Xiao-Jing Liu¹ · Xiang Chai¹

Received: 21 February 2023 / Revised: 11 July 2023 / Accepted: 25 July 2023 / Published online: 21 November 2023

© The Author(s), under exclusive licence to China Science Publishing & Media Ltd. (Science Press), Shanghai Institute of Applied Physics, the Chinese Academy of Sciences, Chinese Nuclear Society 2023

Abstract

Micro-mobile heat pipe-cooled nuclear power plants are promising candidates for distributed energy resource power generators and can be flexibly deployed in remote places to meet increasing electric power demands. However, previous steady-state simulations and experiments have deviated significantly from actual micronuclear system operations. Hence, a transient analysis is required for performance optimization and safety assessment. In this study, a hardware-in-the-loop (HIL) approach was used to investigate the dynamic behavior of scaled-down heat pipe-cooled systems. The real-time features of the HIL architecture were interpreted and validated, and an optimal time step of 500 ms was selected for the thermal transient. The power transient was modeled using point kinetic equations, and a scaled-down thermal prototype was set up to avoid modeling unpredictable heat transfer behaviors and feeding temperature samples into the main program running on a desktop PC. A series of dynamic test results showed significant power and temperature oscillations during the transient process, owing to the inconsistency of the rapid nuclear reaction rate and large thermal inertia. The proposed HIL approach is stable and effective for further studying of the dynamic characteristics and control optimization of solid-state small nuclear-powered systems at an early prototyping stage.

Keywords Micro-heat pipe-cooled nuclear reactor · Hardware-in-the-loop · Dynamic evaluation · Start-up/shut-down processes

List of symbols

C	Precursor concentration
e	Error of the controller
I	Current (A)
P	Power (W)
R	Thermal resistance (K/W)
T	Temperature (K)
t	Time (s)

U	Voltage (V)
u	Output of the controller (–)

Greek symbols

α	Temperature coefficient (K^{-1})
β	Delayed neutron fraction (–)
Λ	Neutron generation time (s)
λ	Decay constant (s^{-1})
ρ	Density (kg/m^3); Reactivity ($\$$)

Subscripts

con	Condenser
e	External
eva	Evaporator
f	Feedback
HP	Heat pipe
i	Group number
inh	Inherent
pv	Process value
ref	Reference

This work was financially supported by the National Key R&D Program of China (No. 2020YFB1901900), National Natural Science Foundation of China (No. 12275175), Special Fund for Strengthening Industry of Shanghai (No. GYQJ-2018-2-02), Shanghai Rising Star Program (No. 21QA1404200), and the LingChuang Research Project of the China National Nuclear Corporation.

✉ Xiang Chai
xiangchai@sjtu.edu.cn

¹ School of Mechanical Engineering, Shanghai Jiao Tong University, Shanghai 200240, China

s	Steady-state
sp	Setpoint

Abbreviations

CD	Control drum
DERS	Distributed energy resources system
HIL	Hardware-in-the-loop
mHPR	Micro-heat pipe-cooled reactor
PKE	Point kinetic equation

1 Introduction

As the construction of electrical power system infrastructure has matured, the corresponding deployment requirements have increased to cover more places and populations. Distributed energy resources (DERs) can help satisfy the power-usage requirements of remote locations by employing microgrid power-generation units [1]. Clean distributed energy generation methods such as wind or solar power are characterized by low carbon emissions and are significant for environmental protection and sustainable development. However, the application of these renewable energy sources is more easily impacted by external conditions and may not stably satisfy variable and flexible power demands [2]. Hence, small-scale nuclear power plants are promising candidates for power generation using DERs, including the proposed conceptual designs that combine solar photovoltaics, thermal energy storage, and nuclear reactors in a hybrid power system [3, 4]. Reactor have solid cores for structural support and use special media to remove the heat released from the fuel. Then, the reactors use the released heat for power generation. This approach can be compactly deployed in a moving container, to serve as a long-life power supply for isolated or remote bases, delivering electrical outputs ranging from kilowatts to megawatts [5].

Based on cooling systems, mobile small nuclear power plants can be divided into heat pipe-cooled and gas-cooled reactors, according to past design experiences. A heat pipe is a high-temperature heat transfer device that leverages the phase transition of the internal working medium to achieve a high efficiency [6]. Unlike in a gas-cooled reactor, the installation of pumps and valves need not be considered in a micro-heat pipe-cooled reactor (mHPR), making it a compact structure suitable for smaller and more flexible applications. In addition, this type of design uses a passive safety mechanism to protect the reactors from extreme accidents. For instance, all heat pipes work independently; therefore, the failure of a single pipe does not have detrimental consequences for the entire system.

Although some conceptual designs have been preliminarily proposed for mHPRs [7, 8], the results of steady-state analyses deviate significantly from actual micronuclear

system operations [9, 10]. In addition, the varying external loadings of the DERs leads to a variable power output from the reactor core during operation. Hence, a transient analysis is necessary for performance optimization and safety assessment in an advanced mHPR design. The coupling effects between neutronics and thermodynamics should be considered for the transient analysis of nuclear systems [11–14]. The power of an mHPR is closely dependent on the neutron population, and the temperature of the system has a significant influence on the geometric deformation and rate of the nuclear reaction. Numerical simulations and physical experiments are typically used to investigate the heat transfer and neutronic dynamics of heat pipe-cooled nuclear systems.

Generally, it is impossible to provide special experimental conditions for neutronic dynamic investigations in laboratory-level engineering. Because the implementation of these neutronic experiments requires material, money, and a site, it is difficult for a scaled-down test bench to accurately represent the real features of a global nuclear system. As an alternative method, theoretical models can be developed [15, 16] and system programs can be implemented [17, 18] to predict the behavior of the entire reactor core. The power level of a nuclear reactor is closely dependent on the evolution of the neutron population, which can be described by the Boltzmann equation, where neutron density is a function of time, spatial location, and energy [19]. In addition, the Monte Carlo method has been widely applied to evaluate the neutronic performance of reactors that involve operate random processes owing to a large number of input particles [20, 21]. Numerical experiments were performed, and the results were consistent with the published benchmarks [22, 23]. This validation proves that the current neutronic numerical model has a high fidelity and is efficient in predicting the power transients of nuclear reactor systems.

However, extensive experimental research has been conducted to provide an authentic viewpoint for the thermal performance of mHPR, by building a small-scale test bench for the target object. For instance, El-Genk [24] measured the temperature time constant of a horizontal water heat pipe and determined its dependence on the rate of temperature change at the beginning of the transient. The start-up process of the heat pipe requires a phase change and transportation of the working medium. Hence, numerous experiments were carried out by considering the heat pipe start-up process for varying evaporator lengths, filling ratios, input powers, inclination angles, and moving conditions [25–28], to determine the heat transfer limit of the device [29]. In addition to conducting experiments on a single heat pipe, it is common to build an integral scaled-down prototype to validate the performance of a conceptually designed mHPR. Such a nonnuclear prototype is mainly composed of a solid matrix, heat pipes, electrical heating rods, and a power conversion system such as a Stirling engine directly connected to a heat

pipe condenser to test the integrated power plant system [30–32]. However, an accurate transient thermal simulation of an mHPR is difficult because of the variation of the geometrical dimensions and gas components of the assembly gap between the fuel and structural material; thus, the heat resistance is difficult to predict [33]. A program capable of precisely describing the transient transport behaviors inside a high-temperature heat pipe has not yet been developed; hence, some simulations use only isothermal boundary conditions for the heat pipe boundaries in multiphysics coupling analyses for simplification [34, 35].

In brief, numerical solutions to transient neutronics equations are reliable; however, the relevant tests are expensive. Although many successful experiments have been conducted on heat pipe-cooled systems, transient heat transfer modeling is inaccurate. Hence, a new hardware-in-the-loop (HIL) method that combines the advantages of both numerical simulations and experiments was employed for the dynamic evaluation of a micro-heat pipe-cooled nuclear system. The HIL was used to feed the measured temperature data from the experimental instrument to a dynamic model running on a software. This approach helps us avoid the transient modeling of heat transfer, leading to resource savings and enhanced efficiency of the software.

HIL have been proposed and successfully used in many other fields for quite some time, such as renewable energy generators, combined heat and power units, and hybrid electric vehicles [36–39]. Considering the nature of the HIL, it can also be considered an important method for controller estimation. Although a real control instrument is extremely complicated, it is easy to use an HIL to optimize a closed-control strategy for a nuclear system. A key point in executing a HIL simulation is to follow the real-time requirements. Because there is always data exchange between hardware and software, it is important to manage the process to maintain synchronous communication. The time step of the HIL is highly dependent on the transient timescale and model complexity. For a high-frequency electromagnetic transient, the HIL simulation should be displayed on a special real-time operating system (OS) running on FPGA or GPU chips [40]. Usually, the temperature variation is much slower, and the characteristic transient is near the millisecond or second level [41, 42]. Hence, a general OS running on a desktop PC can be used to perform soft real-time simulations of nuclear reactor systems.

In this study, an HIL platform was constructed to evaluate the dynamic behavior of an mHPR. We used a one-dimensional neutronic dynamic model to reduce the computational load on a laptop and achieve real-time data exchange. Based on the success of a water heat pipe-cooled DUFF test bench conducted by NASA [30], a scaled-down electrical heating prototype cooled by water heat pipes was constructed for temperature sampling. Water heat pipes have different

working ranges and internal structures compared to alkali heat pipes. Water heat pipes were chosen in this study because they can operate stably and safely at much lower temperatures. As a result, power and temperature transients with a millisecond timescale can be coupled, and their feedback effects can be investigated. Several running scenarios, such as start-up/shut-down and open-loop/closed-loop control, were conducted using the HIL method. The main contributions of this study are summarized as follows:

- A scaled-down thermal test bench for the mHPR was built, and its working performance was evaluated.
- A HIL framework was developed and implemented, and its real-time features were analyzed to determine the best data exchange frequency.
- The dynamic evaluations of the mHPR prototype were conducted under different control patterns based on the HIL method.

The remainder of this manuscript is organized as follows: Sect. 2 presents the details of the dynamic model and test bench. Section 3 describes the combination of these components into a HIL platform, and its real-time evaluation. Finally, in Sect. 4, the test scenarios are listed for a sensitivity analysis of the response behavior of the system, and the simulation results are presented and discussed.

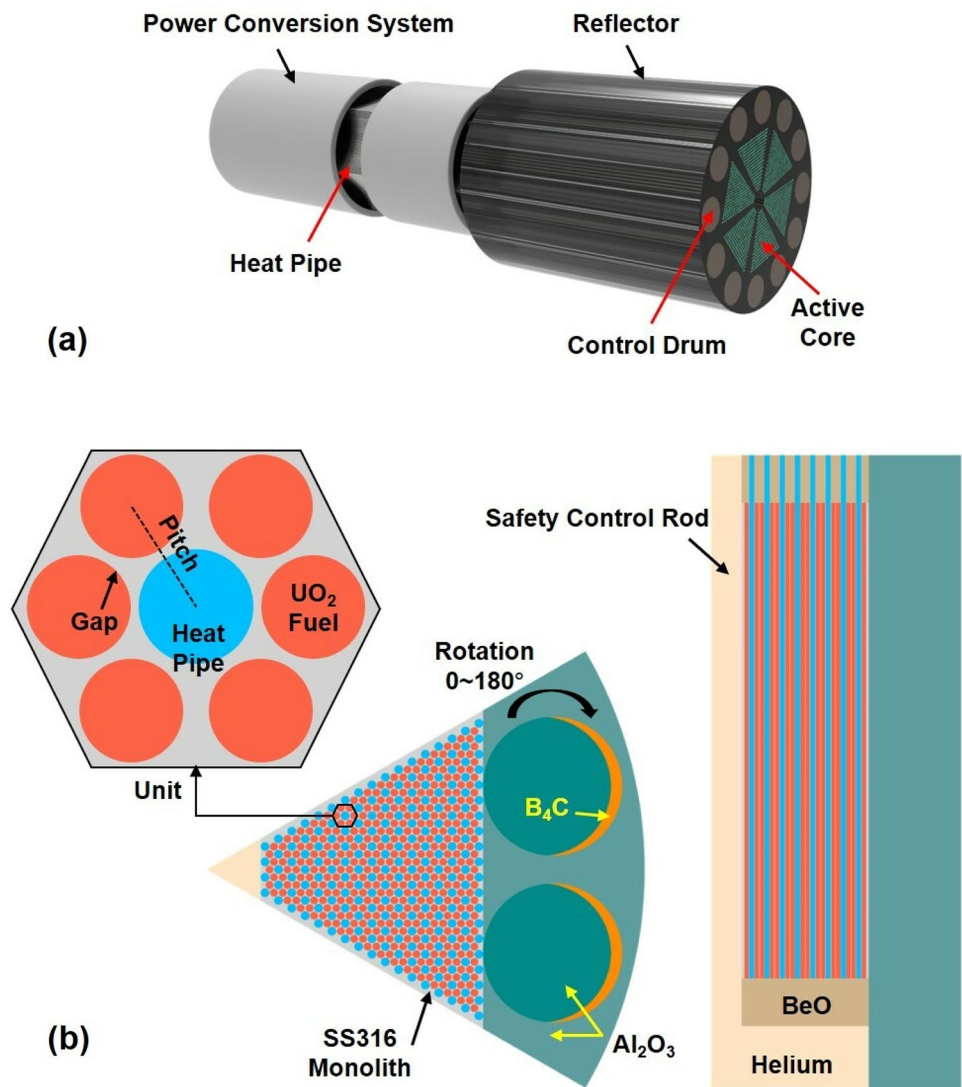
2 Model and method

2.1 Heat pipe-cooled nuclear-powered system

After the micronuclear reactor Kilopower was designed and successfully tested for long-term deep-space exploration, the Los Alamos National Lab (LANL) recently proposed a similar but scaled-up reactor called Megapower [43]. This novel Megapower design offers many advantages. A 5 MW solid-state micro-nuclear reactor was used as the power source, and then the heat was delivered to a power conversion system at the other end by potassium heat pipes. These heat pipes operated at approximately 950 K and demonstrated high heat transfer efficiency.

Figure 1 shows the detailed structure of the reactor core. Many holes were drilled in a SS316 monolith to contain stacked dime-sized nuclear fuel pellets, resulting in a gap of 0.0065 cm between the fuel and monolith; hence, helium fed by the bottom gas plenum filled these gaps. The extra heat resistance caused by these gaps could be critical when determining the heat-transfer performance and spatial temperature distributions of the solid-state core during operation. In particular, the size of the assembly gaps changed because of the thermal expansion of the structural materials or release of fission gas from the fuel, making the gap behavior more

Fig. 1 (Color online) Conceptual diagram of the Megapower nuclear reactor: **a** whole system including the power conversion component and **b** radial and axial layout of the 1/6 reactor core



unpredictable. An alkali metal working medium was filled into the other holes; thus, the heat pipe evaporation section was integral to the SS316 monolith and no gap existed around it. The fuel pin and heat pipe had a hexagonal layout, and the ratio of their total numbers in the core was set to approximately 2:1, to balance the compact dimensions, neutronics, and heat transfer design requirements. Twelve control drums (CDs), which functioned as the main means of power control, were placed lateral to the core [44]. The drums made of B₄C are good at neutron absorption; therefore, the inward rotation of the CDs decreased the reactor power and vice versa.

2.2 Reactor dynamic model

The point kinetic equation (PKE) is a simplified dynamic model in which a nuclear system is regarded as a single point in space, such that the power level is time-dependent. PKE is a set of ordinary differential equations (ODEs) whose numerical

solutions can be easily obtained. The mathematical description of the PKE is as follows:

$$\frac{dP}{dt} = \frac{\rho - \beta}{\Lambda} P + \sum_{i=1}^6 \lambda_i C_i, \tag{1}$$

$$\frac{dC_i}{dt} = \frac{\beta_i}{\Lambda} P - \lambda_i C_i. \tag{2}$$

Here, P , ρ and Λ represent the normalized power, net reactivity, and prompt neutron generation time, respectively. β_i , λ_i and C_i represent the delayed neutron fraction, decay constant, and precursor concentration, respectively, in the i -th group. Although most of the prompt neutrons were released after the reaction, a small portion of delayed neutrons were still produced, making the nuclear power controllable. Based on the PKE, when ρ is equal to β , it is

Table 1 Kinetic parameters used for solving PKEs

Group	$\beta_i (10^{-5})$	$\lambda_i (s^{-1})$	$\beta (10^{-5})$	$\Lambda (s)$
1	23.06	0.0134	757.55	8.04×10^{-6}
2	125.75	0.0325		
3	123.88	0.121		
4	292.74	0.307		
5	135.78	0.867		
6	56.34	2.912		

Table 2 Constants for predicting temperature feedback reactivity

$\alpha_T (K^{-1})$	$T_{ref} (K)$	$\rho_{f,ref} (-)$
0.00731	294	0.05544

defined as 1 \$, and $\rho = 0$ represents the steady state of the investigated system.

The other variables presented in the PKE are called point kinetic parameters and are determined by the reactor configuration. For this research, 1/6 of the Megapower reactor was modeled and simulated using the Monte Carlo code OpenMC [45], as shown in Fig. 1b, to solve these parameters. These values are listed in Table 1.

The net reactivity is divided into two parts, as shown in the following equation:

$$\rho = \rho_e + \rho_f(T_{core}), \tag{3}$$

where ρ_e is the external reactivity caused by the mentioned active CD rotation, and ρ_f is the feedback reactivity related to the temperature variation of the reactor core. In this study, Doppler-broadening feedback was considered.

Based on a pre-conducted Monte Carlo simulation, the correlation between the reactor temperature and inherent reactivity was also obtained. The result suggests a linear relation between $\ln(1 - \rho_{inh})$ and $\ln T$, as shown in the following equation [46]:

$$\alpha_T = \frac{\ln(1 - \rho_{inh}) - \ln(1 - \rho_{inh,ref})}{\ln T - \ln T_{ref}}. \tag{4}$$

Here, the subscript ref means the reference value, and the slope α_T is the Doppler temperature feedback coefficient. These three parameters were constant, and their fitting values are listed in Table 2. Consequently, the feedback reactivity at a certain core operating temperature T_{core} can be solved as follows:

$$\rho_f(T_{core}) = \rho_{inh}(T_{core}) - \rho_{inh}(T_0), \tag{5}$$

where T_0 is the room temperature at the beginning of the system operation.

2.3 Nonnuclear experimental setup and its evaluation

A schematic of the thermal test is shown in Fig. 2, and the key test parameters are listed in Table 3. Electrical heating

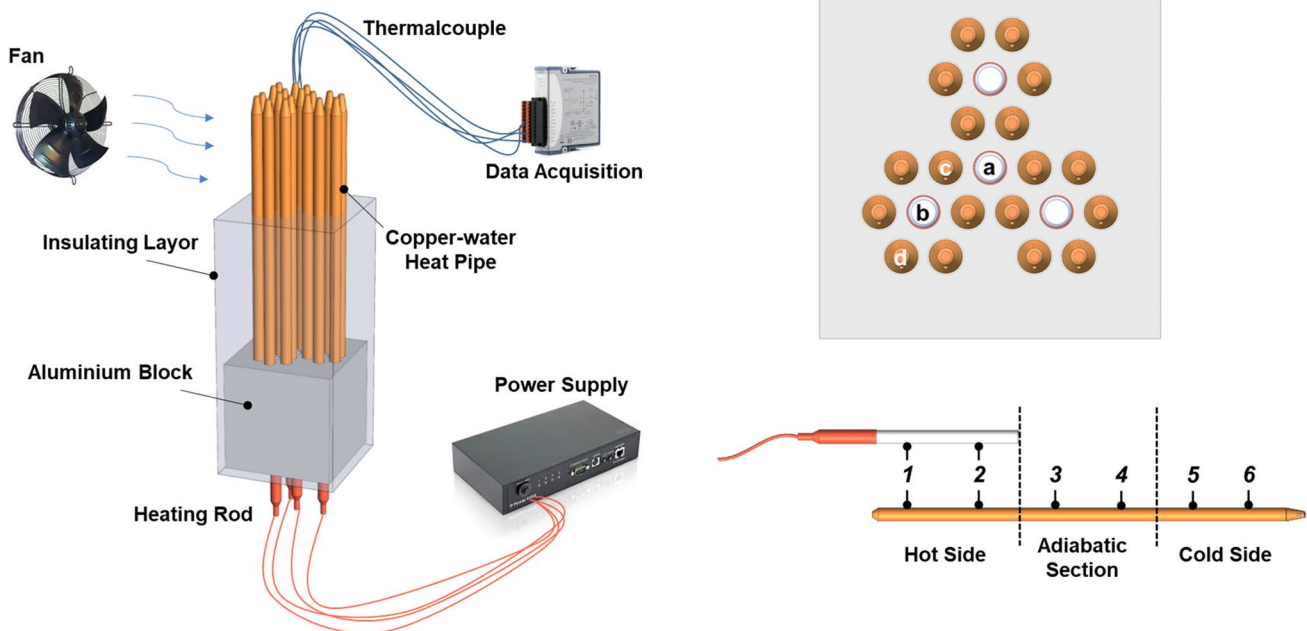


Fig. 2 (Color online) Structure and temperature measurement point of the mHPR prototype

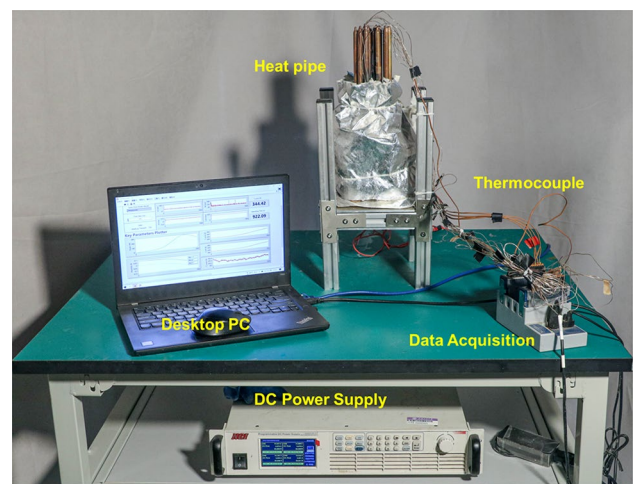
Table 3 Instrumentation specifications

Name	Values
DC power supply	4×60 V/15 A/500 W
Heating rod	
Dimensions	100 mm/φ 9.2 mm/0.5 mm
Output	40 V/400 W
K-type thermocouple	
Diameter	φ 0.6 mm
Operating temperature	< 530 K
Water heat pipe	
Diameter/thickness	Φ 10 mm/0.8 mm
Length	100 mm/140 mm/100 mm
Block	
Edge length	100 mm
Pitch	14.53 mm
Hole diameter for the heating rod	10 mm
Hole diameter for the heat pipe	10.7 mm

rods and water heat pipes were used to imitate the heat released from the nuclear fuel and that removed by the alkali high-temperature heat pipe, respectively. Aluminum is lighter and softer and has a lower processing cost than stainless steel; furthermore, it has a high heat conductivity. Hence, an aluminum block with an edge of 10 cm was fabricated to provide a uniform heating environment. Many holes were drilled to place the heat pipes and heating rods. Eighteen heat pipes and four heating rods were placed in the block in a hexagonal layout; however, the ratio of their numbers was not the same as that of the Megapower reactor. This is because the water heat pipe-cooled system worked at a lower temperature; hence, more heat pipes were required to improve the maximum heat transfer capability of the test bench.

The diameters of the holes in the block were slightly larger than those of the heating rods and heat pipes, which resulted in small gaps of 0.3 mm. Thermocouples were inserted in these gaps to measure the internal core temperature. These gaps can deteriorate the heat transfer between the block and pipes. Hence, these gaps were filled with silicone grease to address this issue. A layer of aluminum silicate was packaged outside the entire facility for thermal isolation, leaving only the top of the heat pipes exposed to the environment for heat exchange and cooling.

The total length of the heat pipe was 34 cm, and the lengths of the evaporator, adiabatic section, and condenser were 10, 14, and 10 cm, respectively. This implies that the reactor and power conversion systems had the same length. These heat pipes were arranged in gravity-assisted orientations to improve the working circulation of the internal

**Fig. 3** (Color online) Photographic of the HIL-based mHPR prototype

medium and effective heat conductivity. The temperature measurement points are shown in Fig. 2. The distances from points 1–6 to the evaporator end were 3, 7, 14, 20, 27, and 31 cm, respectively. We deployed 16 K-type thermocouples on the surfaces of heating rods #a and #b and heat pipes #c and #d. Another four thermocouples were glued to the lateral side of the block to measure the surface temperature. The sheaths of these thermocouples were made of Neoflon PFA, which has good insulation characteristics below 530 K.

In addition, a fan was installed to ensure air convection around the condenser. Two NI 9213 modules operating with NI c-DAQ 9174 chassis were used for temperature data logging. A programmable DC power supply with four independent channels was connected to the heating rod. The output power of these heaters can be controlled using the LabVIEW program. A photograph of the test bench is displayed in Fig. 3.

The thermal resistance of the heat pipe can be defined by the following equation:

$$R_{\text{HP}} = \frac{T_{\text{eva}} - T_{\text{con}}}{P_{\text{input}}/N}, \quad (6)$$

where T_{eva} and T_{con} denote the average temperatures of the evaporator and condenser of the heat pipe, respectively. P_{input} is the total input power. Based on [27], the use of the nominal heat input to evaluate R_{HP} is reasonable because the trends are similar to those of the real R_{HP} , calculated using the actual heat transferred from the heat pipe (P_{trans}). In Eq. (6), N represents the number of heat pipes and has a value of 18.

According to the specifications of the K-type thermocouple, it has an error of 2.2 K. The temperature measurement uncertainty can be calculated using Eq. (7) where $C = \sqrt{3}$ denotes the confidence coefficient. As the minimum temperature during the experimental process was approximately 300 K, the relative error of the temperature measurement was below 0.5%.

$$U_{B,T} = \frac{\Delta}{C} = \frac{2.2}{\sqrt{3}} = 1.27K \tag{7}$$

The error in the supply voltage was 0.05% + 0.1% FS, whereas the error in the current was 0.1% + 0.1% FS. The rated power source range was 60 V/15 A. During the experiments, the maximum value was 32 V/8 A. The relative error of the power can be evaluated using Eq. (8) as follows:

$$\frac{\Delta P}{P} = \sqrt{\left(\frac{\Delta V}{V}\right)^2 + \left(\frac{\Delta I}{I}\right)^2} \tag{8}$$

Hence, the uncertainty of the input power is near 0.37%.

The uncertainty of the heat pipe thermal resistance can be deduced as follows:

$$\frac{\Delta R_{HP}}{R_{HP}} = \sqrt{\left(\frac{\Delta P}{P}\right)^2 + \left(\frac{\Delta(\Delta T)}{\Delta T}\right)^2} \tag{9}$$

Here, ΔT is the temperature difference between the evaporator and condenser. When the input power is low for a heat pipe, ΔT will also be small, resulting in a relatively large error in the calculated thermal conductivity.

After the test bench was built, a series of pretests were conducted to evaluate the heat loss of the entire experimental installation. To achieve this, we closed the fan near the condenser, creating a natural convection environment for cooling. This allowed us to simplify the heat transfer boundary condition of the condenser. The heat loss of the test rig in the environment was evaluated as follows:

$$\text{Heatloss} = 1 - \frac{P_{\text{trans}}}{P_{\text{input}}} (\%), \tag{10}$$

where the heat input (P_{input}) was obtained directly from the DC power source, and the total actual power transferred by the heat pipes (P_{trans}) was evaluated using the radiation and natural convection of the condenser.

$$P_{\text{trans}} = A\epsilon\sigma_B(T_{\text{con}}^4 - T_{\text{air}}^4) + Ah(T_{\text{con}} - T_{\text{air}}), \tag{11}$$

where ϵ denotes surface emissivity and has a value of 0.8 [47], σ_B is the radiation constant, and A is the condenser area of all these heat pipes. The following equation can be used to evaluate the Nusselt number of a vertical pipe undergoing natural convection, when Gr is in the range of $1.43 \times 10^4 - 3 \times 10^9$ [48].

Table 4 Heat loss of the test rig

P_{input} (W)	P_{trans} (W)	$T_{\text{core,s}}$ (K)	Heat loss (-) (%)
60	48.89	368.73	18.5
90	77.75	396.74	13.6
120	104.15	420.16	13.2
150	132.82	442.36	11.5
180	164.59	464.54	8.6

$$Nu = 0.59(Gr \cdot Pr)^{\frac{1}{4}} \tag{12}$$

The heat transfer coefficient h in Eq. (11) can be obtained as follows. The thermal properties of air in Eq. (12) was evaluated using the average values of T_{con} and T_{air} .

To protect the used thermocouples (< 530 K), the power input of the series of heat loss pretests was set within the range of ~ 60 to 180 W, which resulted in a steady-state core temperature $T_{\text{core,s}}$ of ~ 368.73–464.54 K. Based on the results of the pretests shown in Table 4, the heat loss is within 20% when $T_{\text{core,s}}$ is within ~ 368.73 to 464.54 K. The range of the core temperature for the following formal tests with the fan opened (Table 5) is similar to those in the pretests. Because the heat loss of the system is primarily dependent on the system temperature, the heat loss for the formal tests was also regarded as ~ 20%.

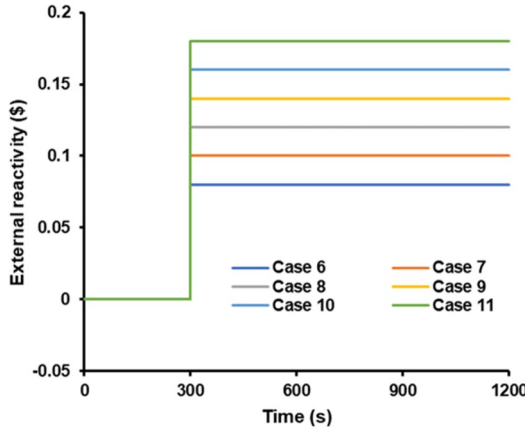
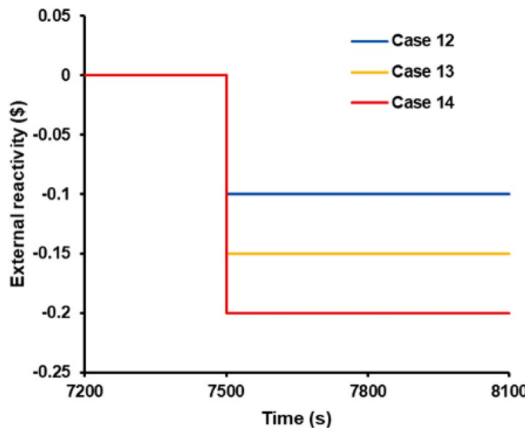
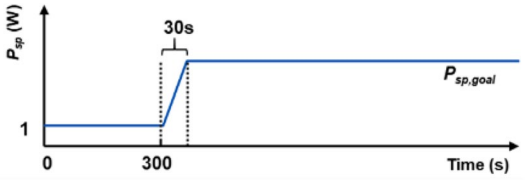
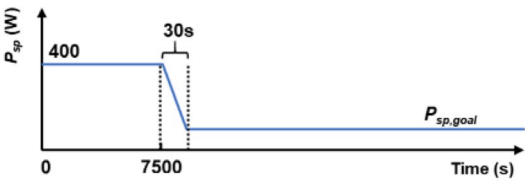
3 Hardware-in-the-loop platform

3.1 System architecture

In the present work, we use a HIL to study the dynamic response of a solid-state reactor, such as the Megapower reactor; the proposed architecture is shown in Fig. 4. As mentioned in Sect. 2, the nuclear system introduction, dynamic model, and scaled-down thermal test setup are demonstrated. Therefore, their combination should be designed and implemented as a functional HIL platform.

The test bench, serving as the hardware, plays a crucial role in sampling temperature data from the real world is a vital component of the dynamic simulation. Ensuring synchronous data exchange between the hardware and software components, especially under transient situations, has been thoroughly considered. The primary components of the hardware side include the main test section, power supply, and data acquisition unit are the hardware parts, as shown in Fig. 2. A LabVIEW program, running in real time on a laptop, served as the software component and was capable of reading the measured data, solving the reactor dynamic equation, and displaying the results, among other functions.

Table 5 Detailed test matrix for both steady-state and transient operations

No	State	Inserted reactivity (ρ)	Power (W)
1	Steady-state	-	100
2			200
3			300
4			400
5			500
6	Transient		Open-loop start-up: initial power is 1 W and updated according to the inserted positive external reactivity and the temperature feedback effect
7			
8			
9			
10			
11	Transient		Open-loop power-down: initial power is 400 W and updated according to the inserted negative external reactivity and the temperature feedback effect
12			
13			
14	Transient	Closed-loop: determine ρ_e based on the on-the-fly power and the PID controller	
15	Transient	Closed-loop: determine ρ_e based on the on-the-fly power and the PID controller	Goal P_{SP} equals the final power of Case 7
16	Transient	Closed-loop: determine ρ_e based on the on-the-fly power and the PID controller	
			Goal P_{SP} equals the final power of Case 13

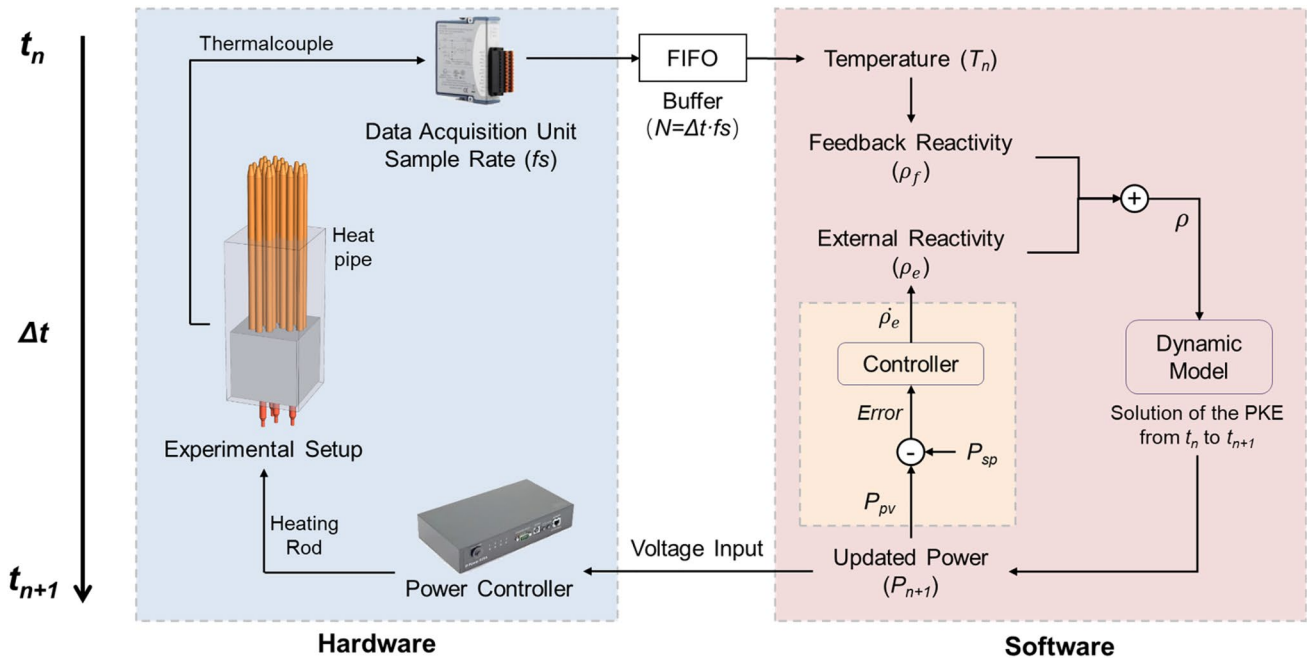


Fig. 4 HIL architecture applied for dynamic evaluation of the mHPR

The data exchange between the hardware and software was facilitated through the simultaneous handling of the power input and temperature measurement. The measured core temperature was used to update the feedback reactivity using Eq. (4).

3.2 Power controller

This program was designed as an optional controller. If a controller is added to the system, a closed-loop simulation is activated, which implies that the external reactivity appearing in Eq. (1) is adjusted by the process power to maintain the power output at the set point. Else, the external reactivity is set as a fixed value to test the power and temperature response features under open-loop operation [49].

A classic PID controller was used in this study because of its stable, effective, and model-free features. Because we built a test bench to determine the thermal response of the nuclear-powered system, the temperature data was periodically sampled from the real world; hence, a digital PID control algorithm was employed. After discretization of the proportional, integral, and derivative actions, the output of the positional PID controller was obtained as a linear combination of these actions, and it can be generally expressed by Eq. (13) [50].

$$u(k) = K_p e(k) + u_1(k - 1) + \frac{K_p}{T_i} \Delta T \left(\frac{e(k) + e(k - 1)}{2} \right) - K_p \frac{T_d}{\Delta T} (PV(k) - PV(k - 1)), \tag{13}$$

where k is one of the sampling points, ΔT is the sample rate, and $u_1(k - 1)$ is the past output of the integral action. u and e are the output and input of the controller, respectively, and e represents the system error.

$$e(k) = SP(k) - PV(k), \tag{14}$$

where SP and PV are the setpoint and process variables, respectively. In Eq. (13), K_p , T_i , and T_d represent the controller gain, integral time, and derivative time, respectively. These parameters work together to determine the controller performance; thus, the parameters should be appropriately tuned before the formal application of the PID controller. Based on the tuning results in this study, K_p , T_i , and T_d were set to 0.012, 0.2 min and 0, respectively.

In this study, a setpoint power (P_{sp}) was applied as the input to the entire system. This error was produced by subtracting the process power (P_{pv}) from P_{sp} . We used this error as the controller input. The reactivity control mechanism of a real nuclear-powered system is significantly more complicated. Therefore, a PID controller was used to simplify the control process and produce the rate of external reactivity insertion as the output u , as shown in Fig. 4.

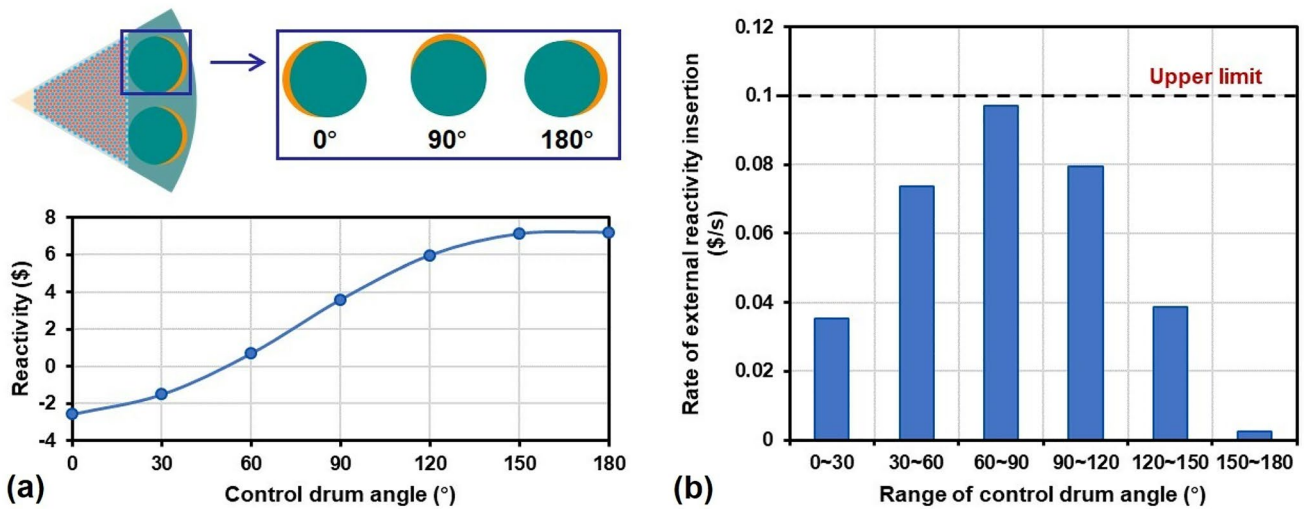


Fig. 5 (Color online) Determination of the upper limit of the rate of external reactivity insertion as the PID controller output, considering a maximum CDs rotation speed of 1°/s: **a** reactivity versus CD angle and **b** rate of external reactivity insertion

As shown in Fig. 5a, with the rotation of the CDs and increase in its angle, the spatial location of the neutron absorption material B_4C gradually moved away from the reactor core, resulting in an increase in the neutron population, external reactivity, and power level. Based on the OpenMC simulation results, the relationship between the calculated reactivity and CD angle is shown in Fig. 5a. A total external reactivity of approximately 9 \$ is added into the nuclear system as the CDs rotate from 0° to 180°. However, the rate of the external reactivity increase is uneven; for instance, this process is faster when the CD angle is approximately 90°. According to past mechanical designs of small solid-state nuclear reactors and CDs, the maximum rotating

speed of CDs should be 1°/s [51]. Therefore, the mean rate of external reactivity insertion among different ranges of the CD angle is shown in Fig. 5b. Here, the maximum value is less than 0.1 \$/s. It is easy to manipulate the rotation direction of these CDs while running. Hence, the output upper limit of the PID controller used here was set as ± 0.1 \$/s to improve the stability of the controller.

3.3 Real-time implementation

Assuming the HIL time step to be 250 ms, the working flow of the software and temperature data treatment during one step are displayed in Fig. 6. The sampling rate of the

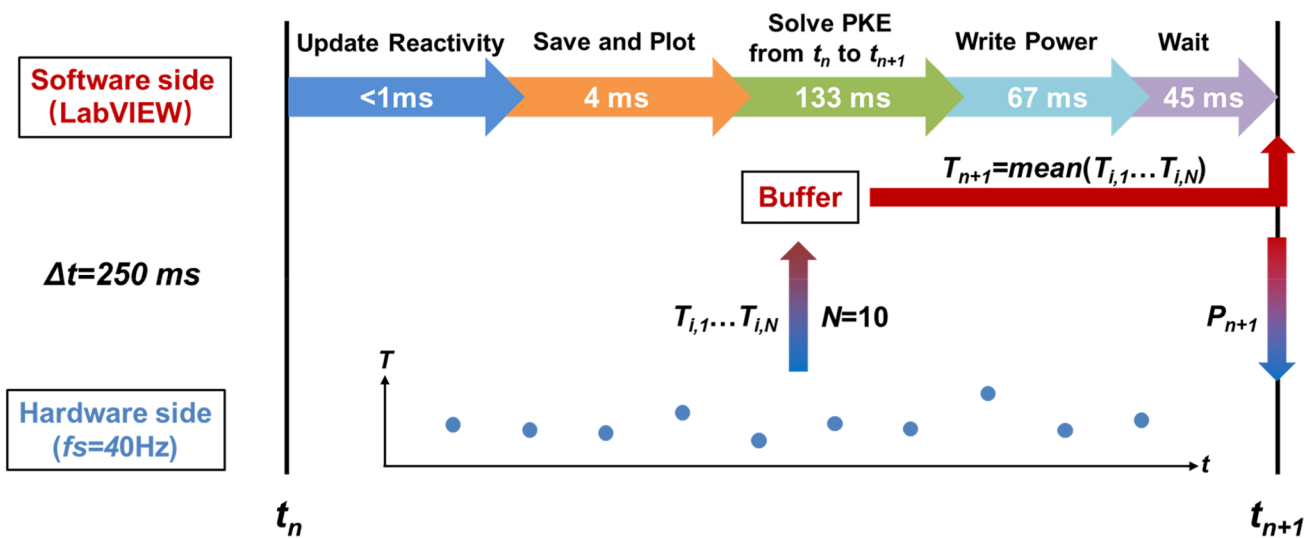


Fig. 6 Real-time feature of the HIL platform for a time step of 250 ms

measurement module was set to 40 Hz, indicating 10 measurement points within one step. These data can be stored in a buffer zone located in the memory of a desktop PC. When the program runs, it removes data from the buffer by following the FIFO principle. An algebraic operation was used to calculate the average value, which represents the average temperature from t_n to t_{n+1} . Under the above treatment, the temperature data can be used in time, and no more than 10 points will be stored in the buffer zone within one step, resulting in a good match between the data measurement and program calculation.

During a single data exchange period, the LabVIEW program mainly had 4 tasks. The first task was preprocessing for the dynamic model simulation, which includes using the measured temperature to update the feedback temperature or adjusting the external reactivity if the PID controller is activated. The remaining three tasks involved data presentation, application of the PKE solution from t_n to t_{n+1} , and delivering the power output to the DC power supply. The numerical solution step for the PKE was set to 1×10^{-4} s to ensure accuracy. For a general operating system such as Windows, the execution time for each task is indeterminate. Figure 6 shows a typical physical time distribution when the step is chosen as 250 ms. These four tasks required 1, 4, 133, and

67 ms. For the first two tasks, the internal calculation in the LabVIEW environment does not involve time cost, whereas the remaining two are relatively time-intensive owing to the potential external communication with the MATLAB ODE solver and DC power supply. In short, the sum of the time spent on the above four tasks should never exceed the set time step to maintain the synchronous performance of the simulation and real-world times. Thus, a wait time of 45 ms was added at the end of the step to account for the discrepancy between these two time-concepts.

Figure 7 shows the front configuration of the program during operation. The top-left part is the control panel, where essential simulation parameters, such as the time step and point kinetic parameters, can be set before running the simulation. The real-time monitor is in the top center zone, and it displays the plot of the time duration for each of the five working tasks in Fig. 6 during a single iteration, along with their summation. The power level, core temperature, and total operating time are listed in the top-right position for notification, in bold. With regard to these key results, their evolutions are presented at the bottom, including the power, reactivity, heat pipe mean temperature, core temperature, and room temperature. In all these plots, the x-coordinate represents the iteration number of the LabVIEW working

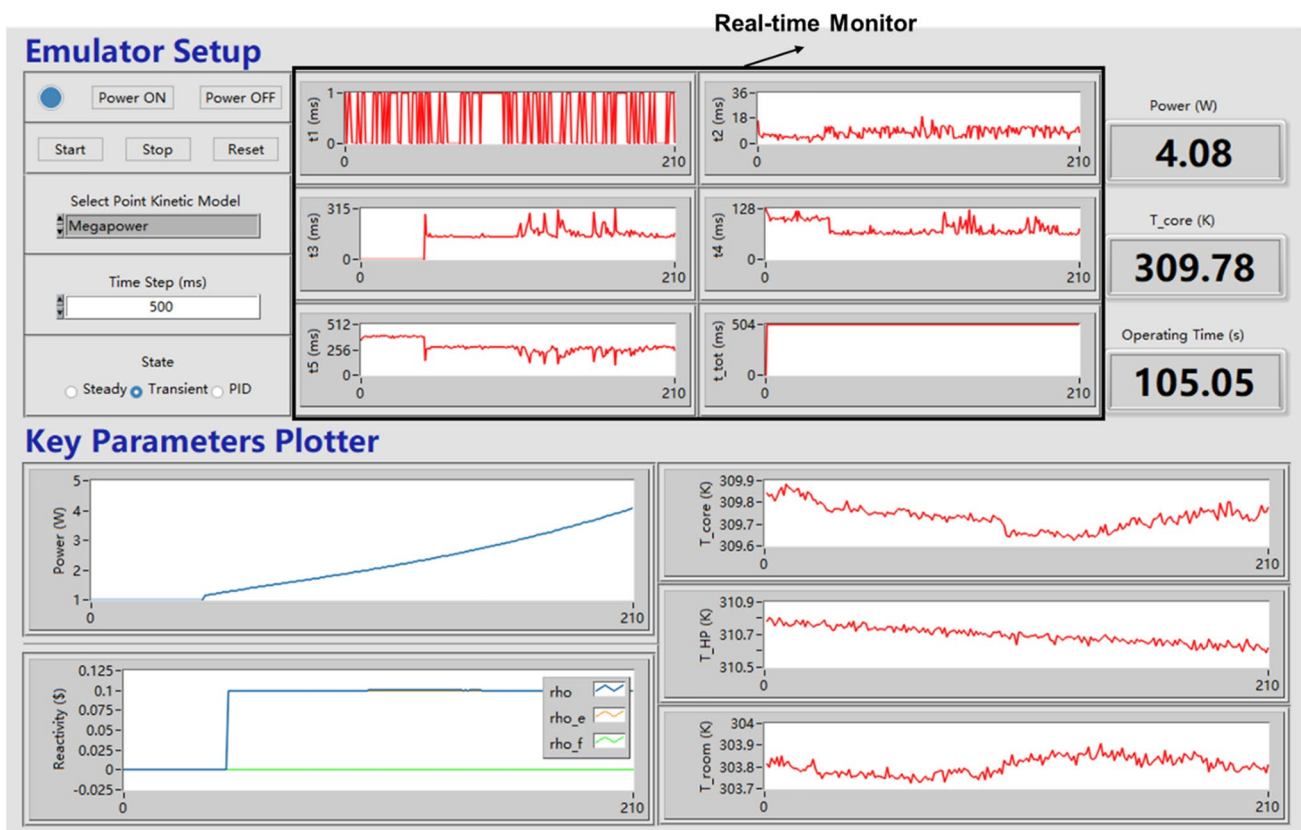


Fig. 7 Screenshot sample of the LabVIEW front panel while running the simulation

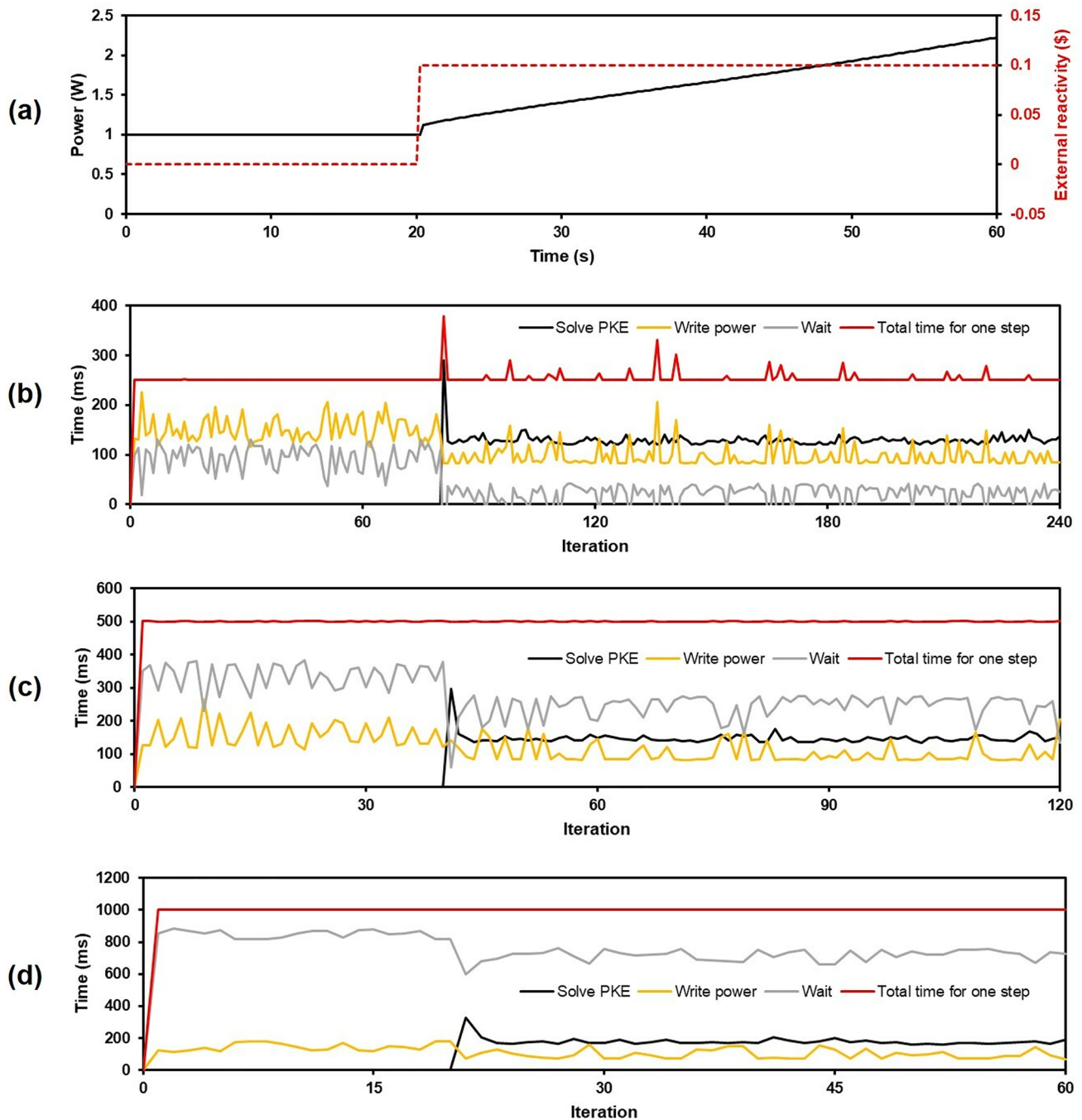


Fig. 8 Real-time performances under different time steps: **a** power and reactivity, **b** 250 ms, **c** 500 ms, and **d** 1000 ms

loop, and the corresponding running time is calculated as the product of the iteration number and HIL time step Δt .

3.4 Performance evaluation of the HIL platform

A sensitivity analysis of the time step was conducted to determine the best level for the current mHPR prototype. As shown in Fig. 6, the time spent solving the PKE was

nearly 100 + ms. Thus, time steps of 250, 500, and 1000 ms were used in this sensitivity analysis, and their performance was evaluated independently.

First, a test scenario was set, as shown in Fig. 8a. In this scenario, an external reactivity of 0.1 \$ was suddenly inserted at 20 s, resulting in the power gradually increasing from the initial value of 1 W. The remaining three subplots in Fig. 8 show the physical time features of the HIL

simulation for different time steps. During the first 20 s, the time required to solve the PKE was costless because the reactivity was zero, and the power was constant. However, for the first iteration after the reactivity was inserted, the solving time jumped to 300 ms, which was mainly attributed to the power prompt jump [49] and activation of the MATLAB node. Subsequently, the solving PKE time was stabilized at 100–150 ms. For all these tests, the time spent writing power to the DC power supply within a single iteration was in the range of 100–200 ms. The accurate value of the execution time was unpredictable because of the nature of the Windows OS. Therefore, the waiting time changed continuously to maintain the total execution time of each iteration within a set time step. As shown in Fig. 8b, a step of 250 ms was inadequate because, at some points, the total execution time exceeded 250 ms because of disturbances,

and thus, the real-time feature was not met. For a time step of 500 or 1000 ms, the total time step was always at the set value, suggesting that a larger time step has a better real-time performance for the HIL platform.

Figure 9 shows another test scenario used in the time-step sensitivity analysis, which considers the controller performance. The initial power was 1 W, and the setpoint of the power exhibited a linear increase in 20–50 s, finally reaching a new steady state at 100 W. The initial external reactivity was zero. From 20 to 30 s, the rate of reactivity insertion quickly reached its upper limit of +0.1 $\$/s$, indicating that the reactivity increased rapidly. During this period, the actual power did not follow the setpoint well as the initial power was low, and the neutron population grew exponentially. After 30 s, the processing power was consistent with that at the setpoint. However, as shown in Fig. 9b the controller output at 1000 ms showed an oscillation at approximately 50 s, but the results at 250 and

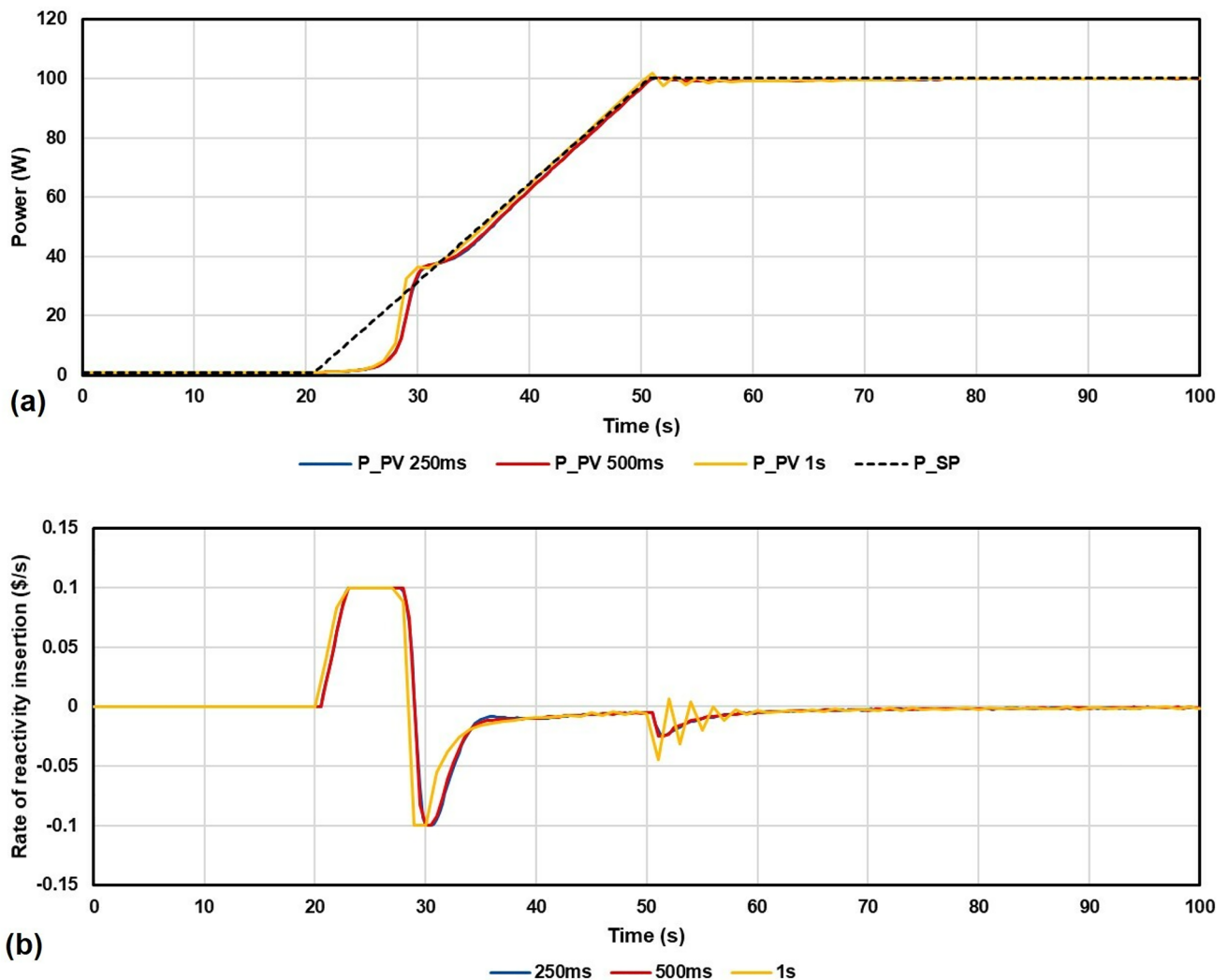


Fig. 9 Power controller performances under different time steps: **a** power and **b** rate of reactivity insertion

500 ms were similar. This test revealed that the time step should be reduced to obtain a better control performance.

Based on the test results, if the time step is too small, the real-time features of the HIL platform can be influenced by the unpredictable execution time of program tasks, such as solving the PKE and writing power. However, if the time step is excessively large, the output of the PID controller becomes unstable because the reactivity and power information cannot be updated in a timely manner. Hence, we chose a time step of 500 ms in the subsequent scenarios, as it represents a good compromise between the real-time and control requirements.

4 Results and discussion

For a real solid-state small nuclear system, a rapid increase in power can occur owing to the exponential growth of the neutron population, even in the case of a small positive reactivity insertion. However, the temperature rise is much slower because of the large thermal capacity of solid structural materials, and the temperature fluctuations significantly influence the nuclear reaction process. Therefore, this system exhibits power-temperature coupling, with different transient response time levels for these two aspects. Based on the developed integral HIL platform, the dynamic response of the mHPR system can be effectively investigated at the laboratory level. Table 5 shows the text matrix of dynamic research, which can be classified into several groups with different conditions and aims.

Cases 1–5 were a series of steady-state experiments with a power of 100–500 W. For these cases, the HIL platform software worked only as a data collection terminal. No reactivity was inserted, and the output power

was constant during the entire process. This could be considered a normal heating/cooling test for a solid core system. The aim of Cases 1–5 was to demonstrate the thermal performance of the test bench, including the temperature distribution, heat pipe thermal resistance, and thermal response time of the system. Therefore, the heat exchange ability and thermal capacity can also be evaluated indirectly.

Cases 6–14 were open-loop transient HIL simulations with fixed external reactivity, and the PKE solver was activated. In these cases, the heating power was automatically regulated using a neutronic dynamic model. Because of the existence of a temperature feedback, power and temperature had interactive effects during the process. Here, we changed the level of the inserted external reactivity to perform a sensitivity analysis of the neutron population variation rate.

Cases 15 and 16 involved closed-loop transient HIL simulations with an additional PID controller. The output power was controlled by following the set point. A linear power-variation process was assumed to occur within 30 s to ensure a stable PKE solution. Thus, the external reactivity was dynamically adjusted to satisfy the power setpoint. For comparison, the target power levels of Cases 15 and 16 were obtained from the results of Cases 7 and 13, respectively.

To ensure consistency, the average room temperature was measured as approximately 305 K for all cases. The fan near the test bench continued working to enable airflow at a speed of 4 m/s to provide a stable and effective heat sink. The forced convection provided by the fan facilitated an increase in the input power to 500 W. Hence, more cases could be investigated while still satisfying the allowable temperature requirement of the thermocouples at 530 K. Furthermore, the forced convection accelerated the heating of the system

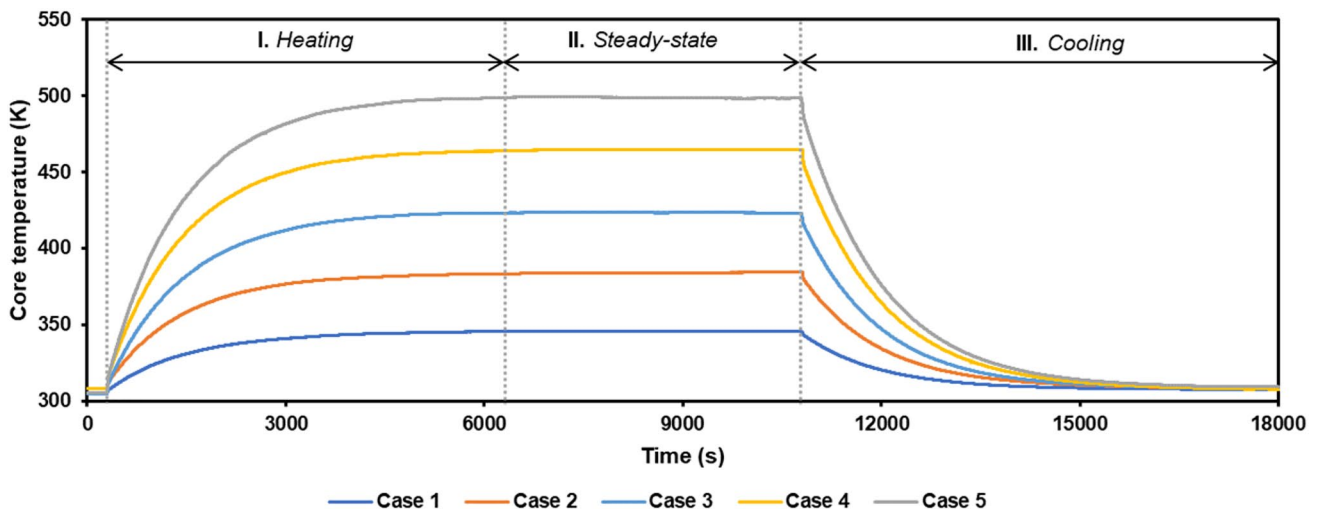


Fig. 10 Temperature variation under a constant power input (the heating was stopped at approximately 180 min)

to establish a steady state. For the start-up cases, the initial external reactivity and power were set as 0 \$ and 1 W. For the shut-down cases, we maintained a constant heating power of 400 W for 7500 s before the formal test, to ensure that a corresponding steady-state temperature had been reached.

4.1 Steady state

Figure 10 shows the experimental results for Cases 1–5 and core temperature evolution process. The core temperature is defined as the mean temperature obtained from the thermocouples located inside the heated block. During the first 6000 s, the core temperature gradually increases to its maximum value, and this period is regarded as the heating period. Then, until 10,000 s, the core temperature remains stable with a disturbance of ± 0.5 K, establishing the steady state. Finally, the external power supply was cut off, and the system temperature decreased to match the environment. The long test period was primarily due to the large thermal capacity of the solid block.

The relationship between the steady-state temperature and power, shown in Fig. 11a, exhibits a strong linear correlation. The average core temperature reached 500 K at 500 W. The results reveal a correspondence between the steady-state temperature of the power and system. For the heating and cooling processes, the concept of the temperature time constant can be applied to describe the speed of the temperature response of the system, whose mathematical expressions are shown in Eqs. (15) and (16) as follows:

$$\Delta T(t) = \Delta T_{ss} \left(1 - e^{-\frac{t-t_0}{\tau_{th,h}}} \right) \tag{15}$$

$$\Delta T(t) = \Delta T_{ss} \left(e^{-\frac{t-t_0}{\tau_{th,c}}} \right) \tag{16}$$

Here, $\Delta T(t)$ is the difference between the current and initial temperatures, and ΔT_{ss} is the difference between the final and initial temperatures. $\tau_{th,h}$ and $\tau_{th,c}$ are the time constants for the heating and cooling processes, respectively. Based on the experimental data shown in Fig. 10, the process temperature difference can be fitted using Eqs. (15) and (16), and the resulting values of $\tau_{th,h}$ and $\tau_{th,c}$ under different powers are plotted in Fig. 11b. This indicates that the temperature–time constant of this system is in the range 1000–1200 s. Owing to the form of the temperature response described by Eqs. (15) and (16), the total heating and cooling times for all these cases were similar, as shown in Fig. 10. Hence, it can be concluded that the solid-state system temperature variation behavior is hardly affected by the constant power, and the thermal response of the system is relatively slow owing to the large thermal capacity with a temperature time constant of approximately 1100 s.

The operating performance of the water heat pipe under steady-state conditions is shown in Fig. 12. The axial temperature distribution was even for all cases. The temperature difference between the evaporator and condenser was approximately 10 K for Case 5, with a power input of 500 W. As shown in Fig. 12b the thermal resistance of one of the heat pipes was ~ 0.4 K/W, based on Eq. (6). Furthermore, the thermal resistance decreased as the power increased. This

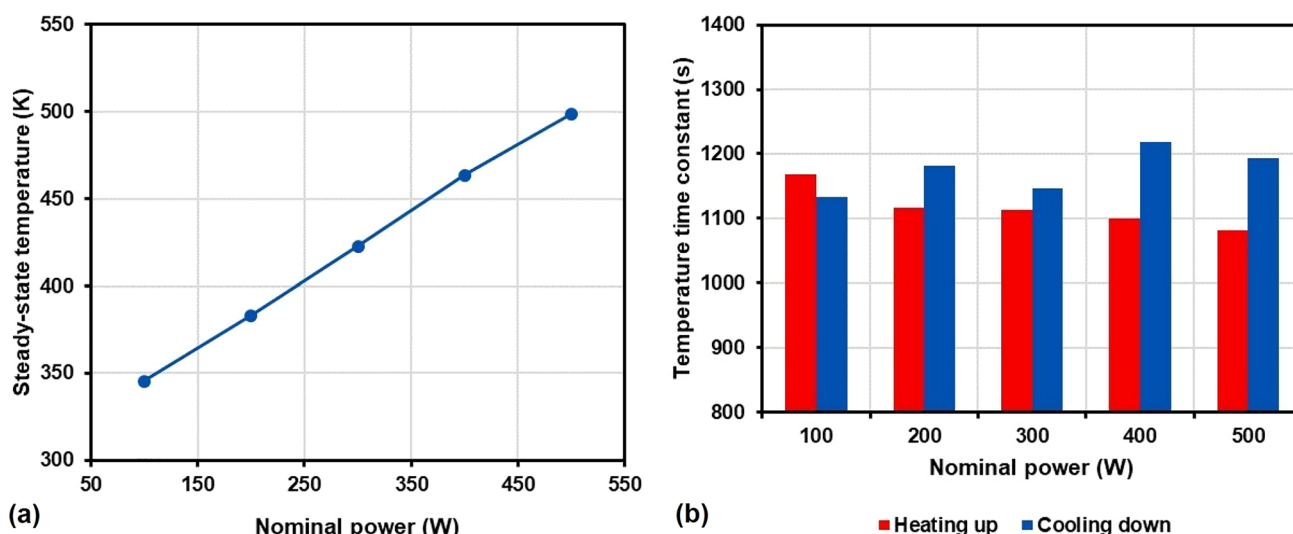


Fig. 11 (Color online) Time response of the heat pipe-cooled system under different input power: a steady-state temperature and b temperature time constant

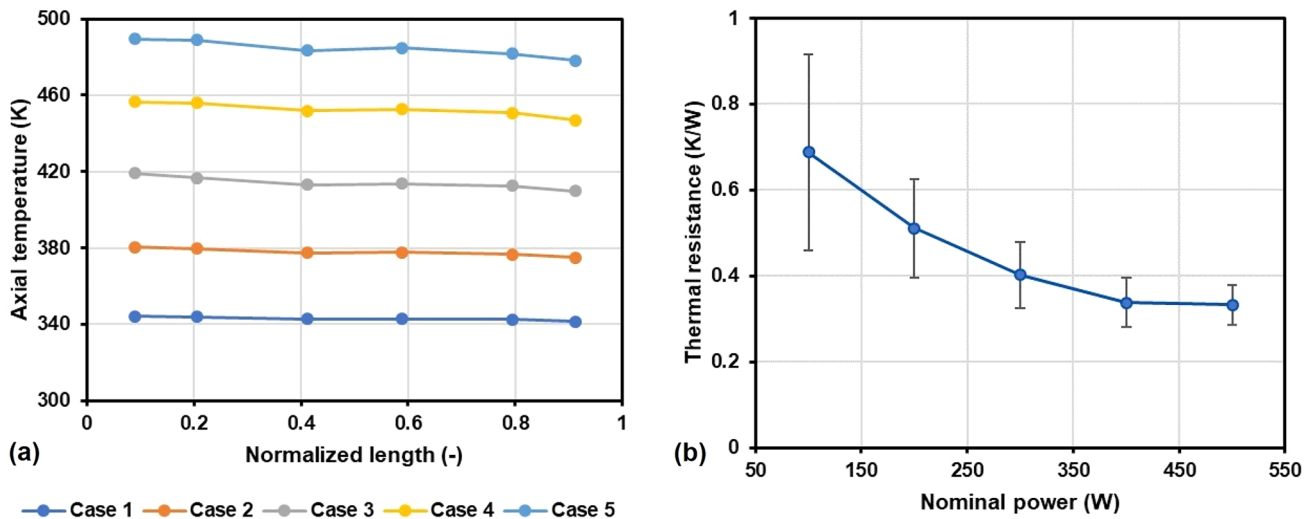


Fig. 12 Heat pipe heat transfer evaluation under different power inputs: **a** axial temperature distribution and **b** thermal resistance of a heat pipe

phenomenon is consistent with previous studies [52], which suggested that higher power improves the heat removal capability of the heat pipe. The uncertainty of the thermal resistance at a lower power level is much larger owing to the reduced temperature difference between the evaporator and condenser. In short, these heat pipes have an excellent heat transfer capability, with an effective thermal conductivity of up to 4000 W/m K.

4.2 Start-up transient

Figure 13 shows the startup process of Case 7, where we insert a step external reactivity of +0.1 \$ at 300 s. Figure 13a shows the variations in power and temperature. This positive external reactivity is compensated by the negative feedback reactivity caused by the temperature growth, such that a new steady state can eventually be established under a net reactivity of zero. As shown in Fig. 13a, the intermediate process exhibits relatively complicated power and temperature oscillations, which can be explained by the unmatched time transient of the neutronics and thermal dynamics. A similar phenomenon has been previously reported [53]. The slow temperature increase at the beginning caused a significant power overshoot. The peak power rapidly emerged because of the exponential neutron growth. The high power accelerated temperature growth, resulting in a temperature overshoot. After passing through another much lower peak, the oscillation gradually vanished, indicating the establishment of a dynamic balance among reactivity, power, and temperature.

The variation in the wall-temperature distribution of heat pipe #c in Case 7 is shown in Fig. 14. The wall

temperature difference between the evaporator and condenser is within 3.5 K during the start-up transient. Based on [24], the variation in the axial vapor temperature is within 0.9 K for water heat pipes; thus, the wall temperature has a positive relationship with the wall heat flux. In this study, only the evaporator heating power was controlled and varied, whereas the condenser was cooled by natural convection and radiation. It can be found from the plots that the transient variation of ΔT_{a-c} has a similar oscillation trend with the power, meaning that heat pipes have better isothermal characteristics and the temperature difference between the reactor and the power conversion system is flattened when the heating power is decreasing.

During the sensitivity analysis of Cases 6–11, similar power and temperature oscillations were observed using the HIL test bench. In the theory of neutronics, the stable exponential power growth after a step of external reactivity is inserted can be approximated using Eq. (17).

$$P(t) = AP_0 e^{\frac{t}{\tau_n}}, \quad (17)$$

where A is a proportionality coefficient, and P_0 is the initial power. τ_n is defined as the neutronics period, which means the time needed for the power to change by e times. Table 6 lists the calculated neutronics period of Cases 6–11. As the external reactivity increases, the neutronics period decreases rapidly, and the power increases in the nuclear-powered system. For Case 11, a neutronics period of 31.61 s means that it only needs 72.8 s for the power to increase by an order of magnitude. However, the temperature time constant, shown in Fig. 11b, is approximately 1100 s, which is much lower than the rate of power increase. This discrepancy could offer

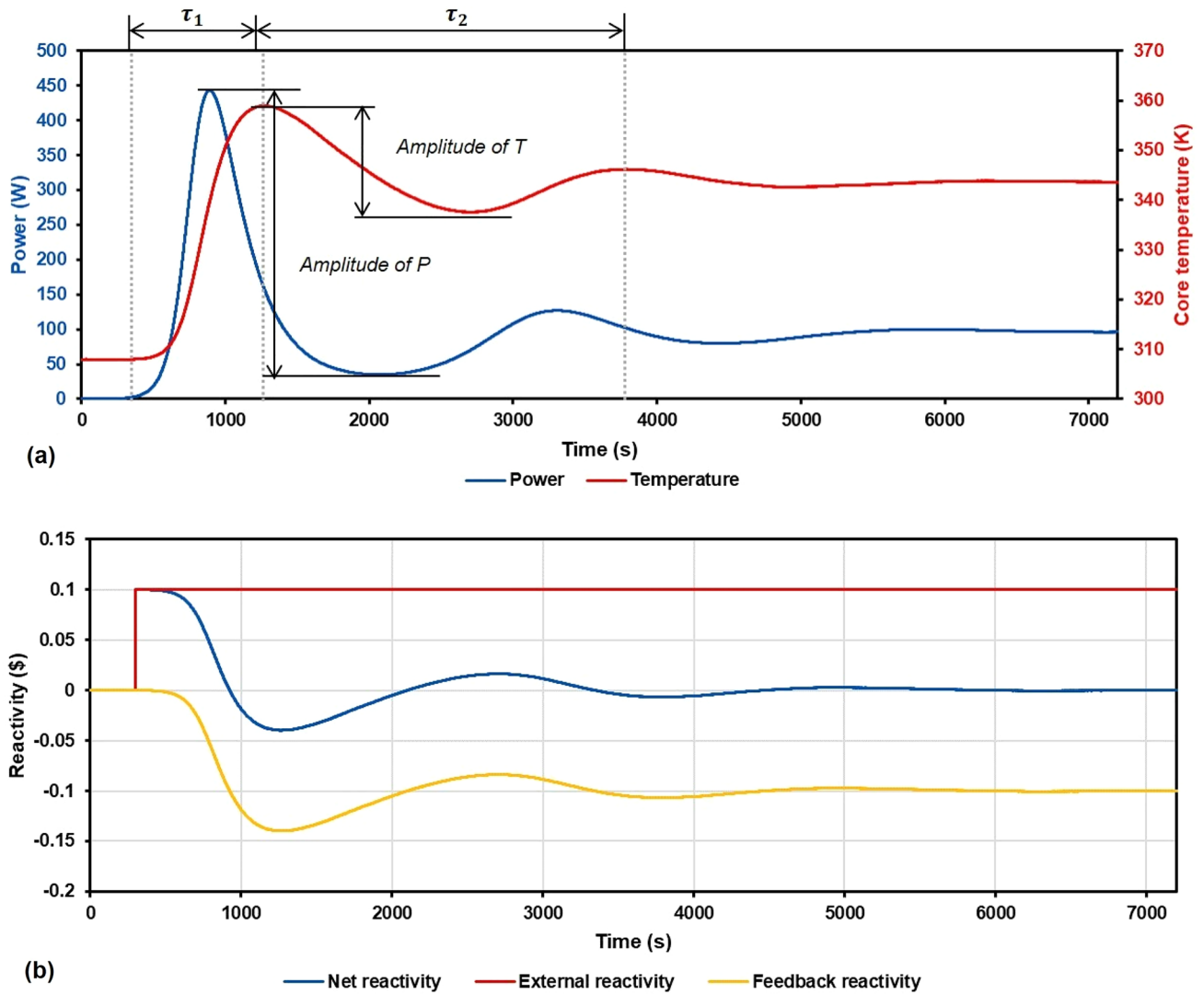


Fig. 13 Results of Case 7 with an external reactivity step of +0.1 \$ inserted: **a** power and temperature and **b** reactivity

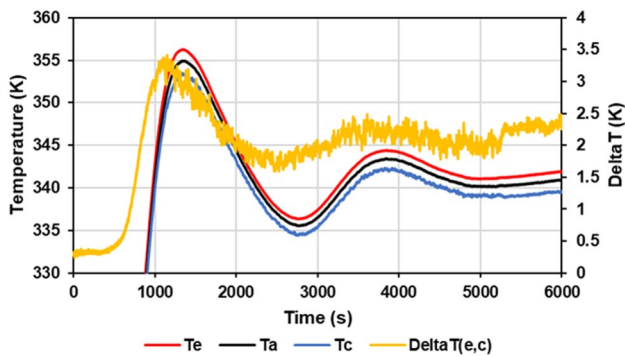


Table 6 Neutronics period for Cases 6–11

No	Step external reactivity (\$)	Neutronics period (s)
6	+0.8	97.16
7	+1.0	73.05
8	+1.2	57.23
9	+1.4	46.08
10	+1.6	37.88
11	+1.8	31.61

Fig. 14 Variation of the wall temperature distribution of the heat pipe #c in Case 7

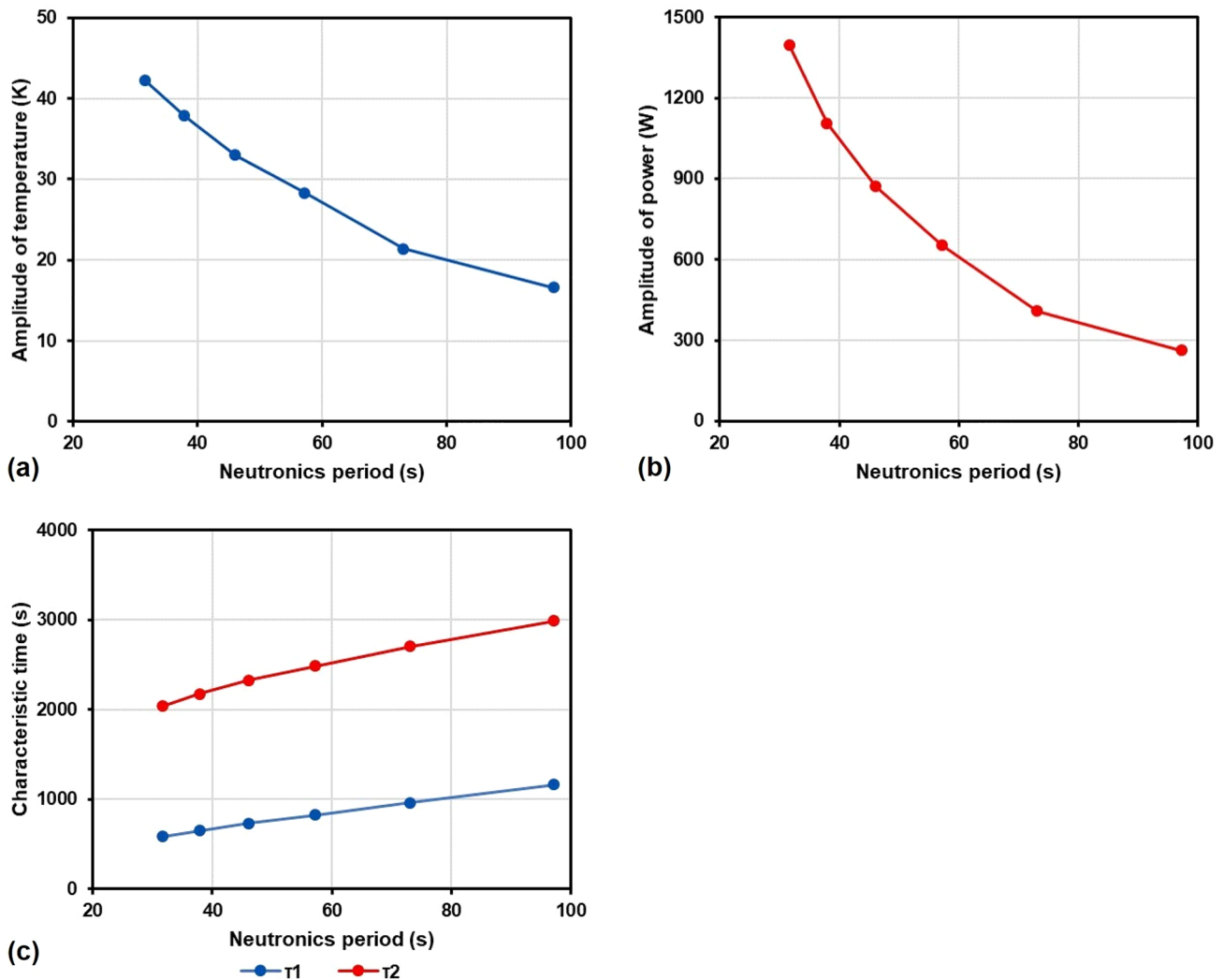


Fig. 15 Oscillation phenomena of temperature and power as functions of neutronics period: **a** amplitude of temperature, **b** amplitude of power, and **c** characteristic time

a quantitative interpretation of the oscillations observed in solid-state nuclear systems.

To investigate the nature of the oscillations, we utilize the characteristic times τ_1 and τ_2 , along with the amplitudes of power and temperature, as defined in Fig. 13a. This allows for a comprehensive description of both the duration and strength of the oscillations. The relationship between the external reactivity and neutronics period is displayed in Table 6 for open-loop Cases 6–11. As the net reactivity changes with temperature, the inserted external reactivity is used to represent the transient features of the system. The initial external reactivity reflects the rate of neutron multiplication. The trends in these characteristic parameters, as functions of the neutronics period, are shown in Fig. 15. As the external reactivity increases and neutronics period shortens, the first overshoot (τ_1) seems to occur earlier, and the amplitude of oscillation increases. In addition, the oscillations

during long neutronic periods lasted longer. Figure 15c demonstrates a strong linear correlation between the characteristic oscillation time and neutronics period. Notably, the power overshoot was much more severe than the temperature overshoot. Taking Case 11 as an example, the amplitude of the power reached 1200 W. Consequently, the oscillations following a substantial external reactivity insertion must be carefully monitored in the rapid start-up scenarios to protect the reactor core from the impact of intense power and thermal transients.

To eliminate the oscillations observed in Cases 6–11 during the power-up process, a closed-loop operation and controlled external reactivity insertion were adopted in Case 15, which resulted in the key parameter evolution shown in Fig. 16. As mentioned in Sect. 3, the time step of the data exchange and operation of the PID controller was set as 500 ms. The power setpoint was chosen to linearly increase

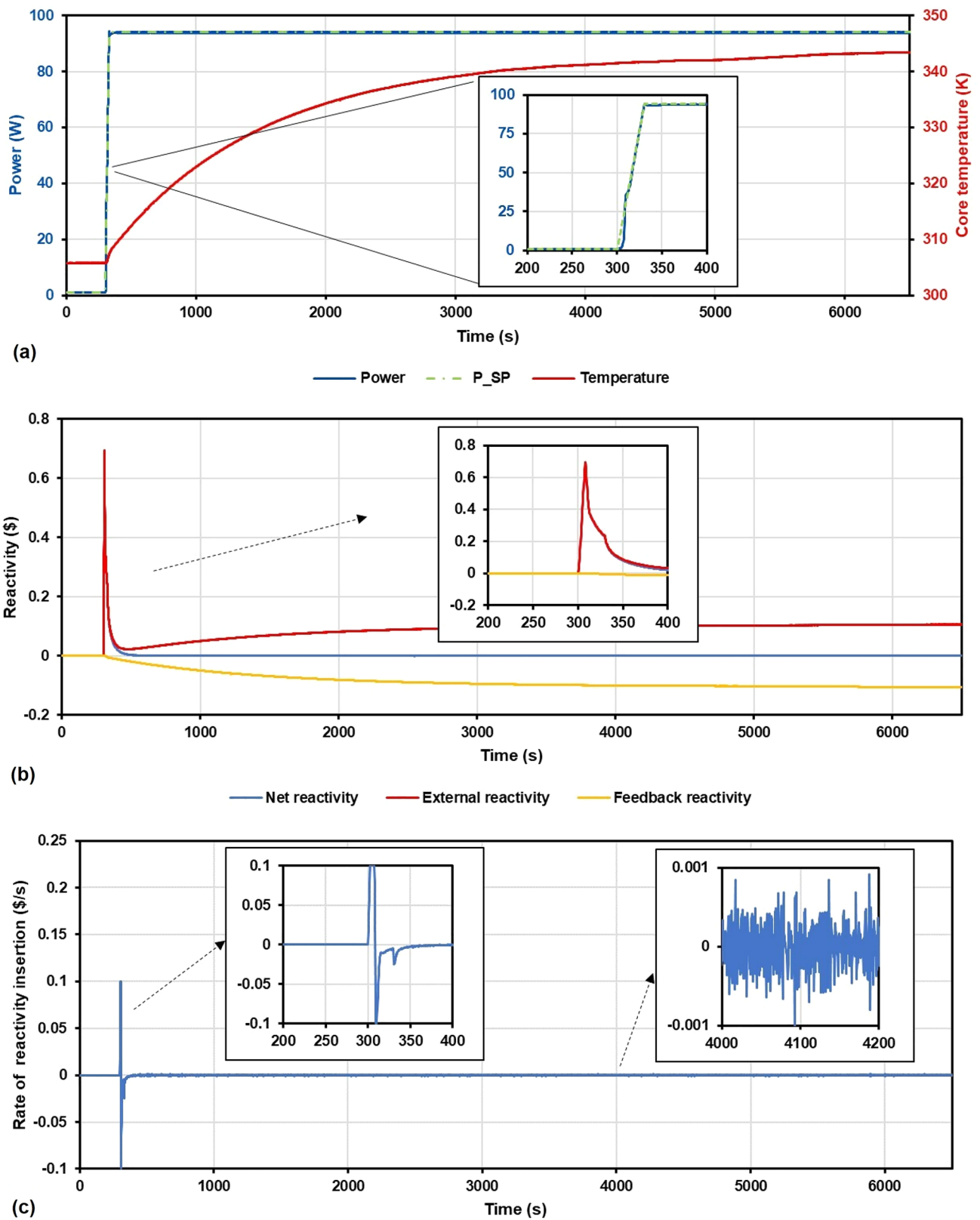


Fig. 16 Results of Case 15, with a PID controller. The target steady-state power matches that obtained in Case 7. **a** Power and temperature, **b** reactivity, and **c** rate of external reactivity insertion

from 1 to 94 W during the time period from 300 to 330 s. Hence, the rate of power increase was 3.1 W/s. As seen in Fig. 16a, the process power can generally follow the setpoint well, thereby affirming the effectiveness of the controller. As seen in Figs. 16a–c, the rate of reactivity insertion quickly reached its upper limit of $+0.1 \text{ } \$/\text{s}$ at 300 s, resulting in an increase in the external reactivity to 0.7 $\$$, indicating that no prompt criticality occurred and that the nuclear system was safe. The power also increased from 1 to $\sim 35 \text{ W}$ under this large external reactivity. Subsequently, the rate of reactivity insertion suddenly decreased to its lower limit of $-0.1 \text{ } \$/\text{s}$ to ensure that the power followed the setpoint. This sudden change in the controller output indicates a variation in the direction of the CD rotation during real-time operation. Subsequently, over the course of 330 s, the CD slowly rotated inward to maintain the power linearly at 95 W. During the initial power-up period, the temperature fluctuations were

not pronounced; therefore, the net reactivity was almost equal to the external reactivity. After 400 s, the CDs were controlled to gradually insert an external reactivity to compensate for the negative feedback reactivity caused by the core temperature growth; thus, the power could remain at 95 W under a zero net reactivity. During this period, the rotation of the CD was quite slow; therefore, a dead zone should be applied to the controller to prevent frequent movement of the CDs and protect its actuator instrument under real-world applications. During the entire process, the core temperature increased smoothly to its steady state, and no oscillations appeared owing to the contribution of the controller.

4.3 Shut-down transient

In addition to the start-on transient, a series of shut-down analyses was conducted in this study because small nuclear

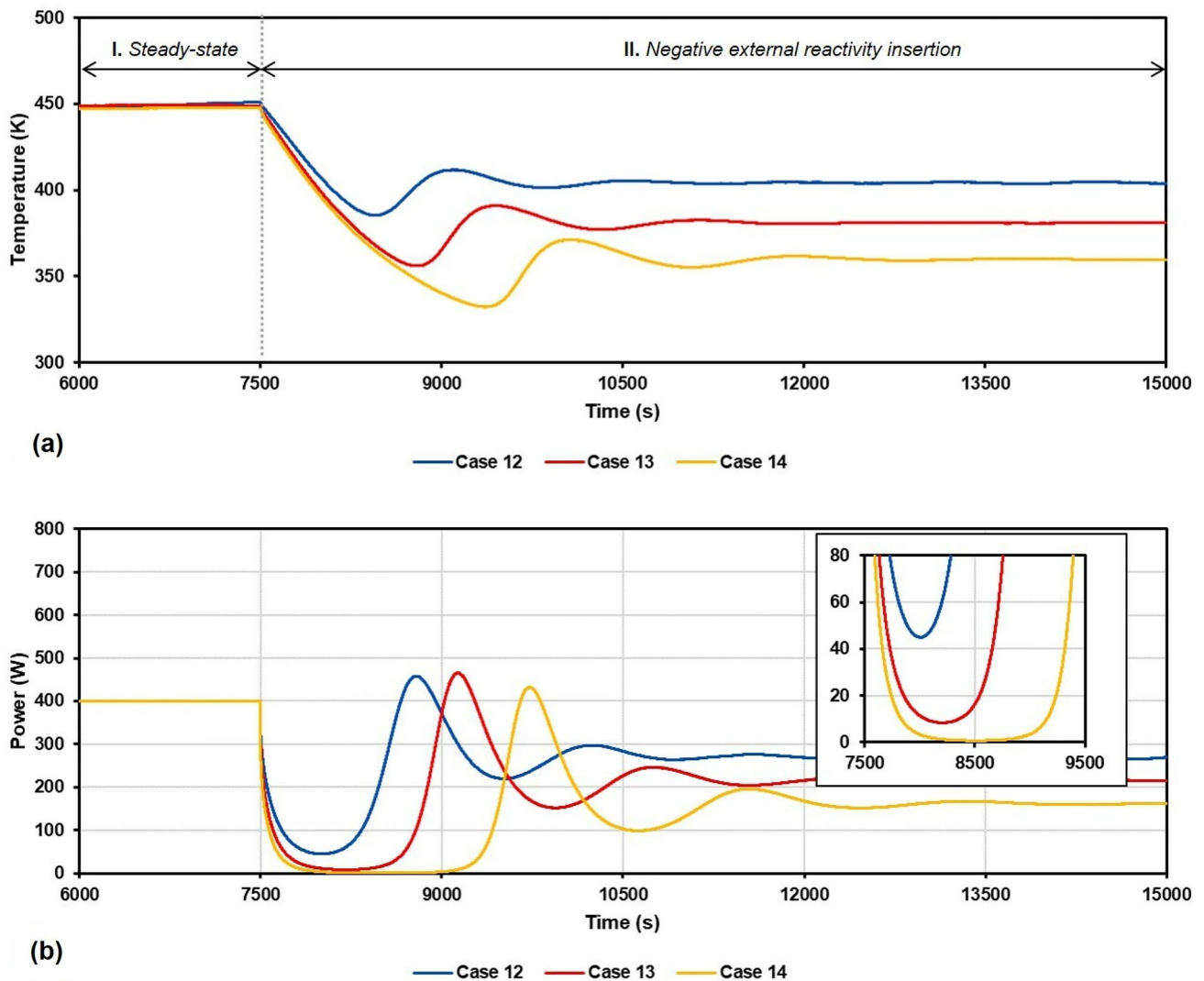


Fig. 17 Power and temperature overshoot in Cases 12–14: **a** temperature and **b** power

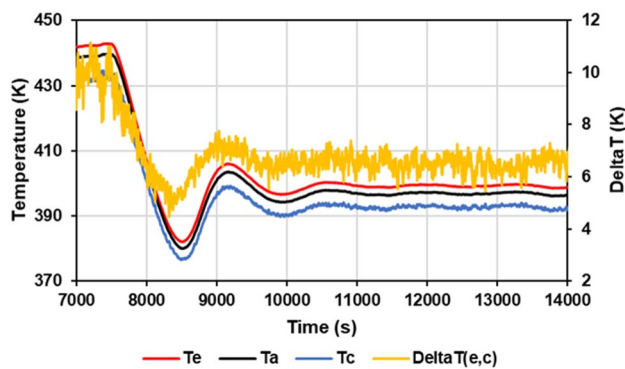


Fig. 18 Variation of the wall temperature distribution of the heat pipe #c in Case 14

reactors often need to accommodate flexible power output requirements. Figure 17 shows the HIL simulation results for the open-loop power-down processes for Cases 12–14. The initial power was 400 W, and the preheating process lasted for 7500 s until the core temperature stabilized at approximately 450 K. During the first 1000 s after the negative step, external reactivity was inserted, causing a rapid decrease in the power, which dropped below 50 W. However, a significant power occurred in all these cases because of the rapid temperature drop, leading to a positive net reactivity at 8000–9000 s. The power peak reached 450 W, which was even higher than the initial power, was attributed to the large initial neutron density. Oscillations also emerged during the power-down process when considering the temperature feedback. In different cases, the amplitudes of these oscillations were quite similar, but the oscillation duration significantly increased as the inserted negative external reactivity increased. After 11,000 s, this oscillation gradually vanished, and the system reached a new steady state.

The variation in the wall temperature distribution of heat pipe #c in Case 14 during the shutdown process is shown in Fig. 18. Similar to the start-up process, the axial temperature difference of the heat pipe varies with the heating power, and ΔT_{a-c} drops from 10 to 6 K. The temperature distribution between the reactor and power conversion system appeared to be more uniform after the heating power, and the heat flux outside the evaporator decreased.

The final stable power of Case 13 was 205 W, which was used as the target set point for Case 16. In Case 16, the PID controller was adopted, and a closed-loop simulation was conducted. The evolution of these key parameters in Case 16 is shown in Fig. 19. Over a span of 7500 s, the power setpoint decreased at a rate of -6.5 W/s, and the controller output promptly adjusted to -0.01 $\$/s$, resulting in an external reactivity of -0.2 $\$$. Subsequently, the CD reversed and rotated outside, providing a positive external reactivity of $+0.012$ $\$/s$. Thus, the reactivity were controlled to

maintain the process power following the setpoint. As per the results shown in Fig. 19a, the controller demonstrated excellent performance, and no temperature oscillation was observed, in contrast to the results of Case 13. This test revealed the effectiveness of the closed-loop operation in regulating the power-down process and emphasized the importance of precise control over the external reactivity by adjusting the angles of the drums. This outcome is consistent with that discussed in the startup simulation in Sect. 4.2.

5 Conclusion

In this study, we designed a HIL framework to investigate the dynamic response of a solid-state mHPR system. The HIL platform was based on a general desktop PC with a special real-time treatment, and a scaled-down prototype of the proposed mHPR was built in the laboratory. Using this HIL simulation, complicated nuclear systems can be tested and researched with high efficiency and low capital costs because no expensive real-time target hardware or experimental materials are involved. Many simulations, including start-up/shut-down and open/closed-loop controls, were carried out, and their results were discussed. The main conclusions are summarized as follows:

- (1) To address the execution time disturbance caused by the desktop PC OS, a buffer zone with a FIFO mechanism was used for data synchronization between the hardware and software. Sensitivity analysis indicated that choosing 500 ms as the HIL time step could achieve a good compromise between the real-time and control requirements.
- (2) The thermal features of the test bench were evaluated using a constant power input. The heat loss in the experimental setup was less than 20%, and the temperature time constant was approximately 1100 s. The water heat pipe exhibited excellent heat transfer performance, with an effective thermal conductivity of up to 4000 W/m·K.
- (3) In open-loop system operation, significant power and temperature oscillations were observed after a step external reactivity was inserted. During the start-up process, the oscillation characteristic time had a linear relationship with the neutron period. During the shutdown process, the oscillations lasted longer as the external reactivity of the inserted negative step increased. These oscillations can be explained by the inconsistency of the transient time level between the neutron reactions and temperature variations in a solid-state nuclear system with large thermal inertia. This phenomenon should be taken into account in the real design process.

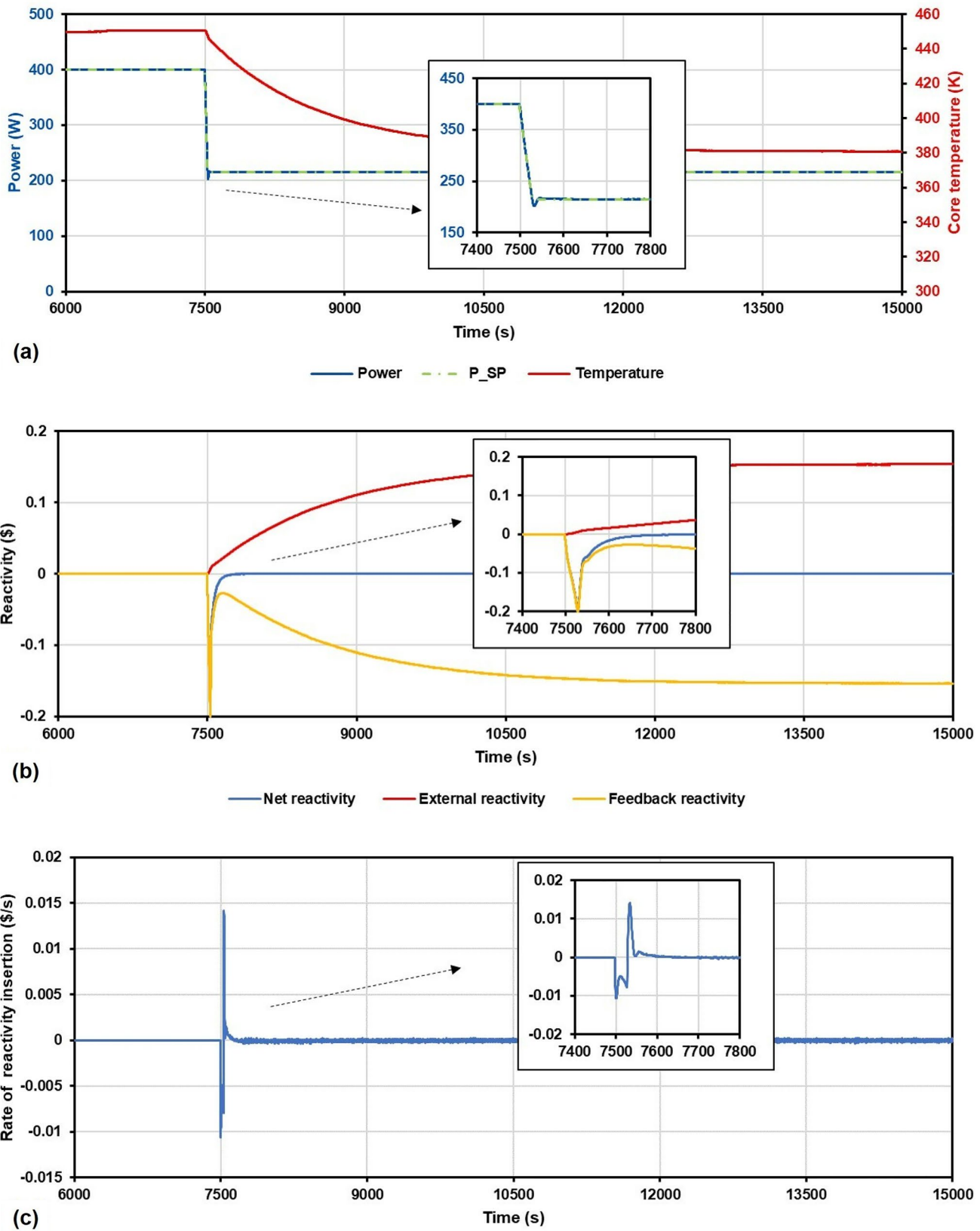


Fig. 19 Results of Case 16 with a PID controller involved. The target steady-state power was set based on the result obtained in Case 13. **a** Power and temperature, **b** reactivity, and **c** rate of external reactivity insertion

- (4) The closed-loop controller helps eliminate oscillations by adjusting the CD rotation speed and direction. When the required external reactivity insertion is small, a dead zone should be considered in the real control system for better power following and protection of the CD structure.

Notably, there are differences in the dynamic characteristics between this study and the actual operation of heat pipe-cooled nuclear reactors. The frozen start-up of high-temperature alkali heat pipes results in a rapid temperature increase from room temperature to above 700 K, enabling the establishment of a steady continuum vapor flow. This requires more complicated operating schemes for managing the external reactivity. Moreover, the size and thermal inertia of the actual solid core were significantly larger than those of the prototype. This could have caused the slower variation in the core temperature and different oscillation periods. In addition, the thermal expansion of the solid core significantly contributes to the negative temperature feedback effect and should be included in the transient analysis.

In future work, this HIL platform could be improved in many aspects, such as using a high-temperature heat pipe to closely replicate the real core temperature, enlarging the dimensions of the test bench to investigate the influence of the power spatial distribution, considering the thermal–mechanical feedback effect, and replacing the PKE with a more complicated but accurate neutronics model. In summary, the initial HIL platform proposed in this study has proven effective in characterizing the dynamics of small solid-state nuclear-powered systems and shows promise for further exploration.

Author contributions All authors contributed to the study conception and design. Material preparation, data collection and analysis were performed by Jiao-Long Deng, Tian-Shi Wang and En-Ping Zhu. The first draft of the manuscript was written by Jiao-Long Deng and all authors commented on previous versions of the manuscript. All authors read and approved the final manuscript.

Data availability The data that support the findings of this study are openly available in Science Data Bank at <https://doi.org/10.57760/sciencedb.j00186.00272> and <https://cstr.cn/31253.11.sciencedb.j00186.00272>

Declaration

Conflict of interest The authors declare that they have no competing interests.

References

1. J. Wang, A. Pratt, K. Prabakar et al., Development of an integrated platform for hardware-in-the-loop evaluation of microgrids prior to site commissioning. *Appl. Energ.* **290**, 116755 (2021). <https://doi.org/10.1016/j.apenergy.2021.116755>
2. G. Bayrak, E. Kabalci, Implementation of a new remote islanding detection method for wind-solar hybrid power plants. *Renew. Sust. Energ. Rev.* **58**, 1–15 (2016). <https://doi.org/10.1016/j.rser.2015.12.227>
3. B.C. Zhao, M.S. Cheng, C. Liu et al., Conceptual design and preliminary performance analysis of a hybrid nuclear-solar power system with molten-salt packed-bed thermal energy storage for on-demand power supply. *Energ. Convers. Manage.* **166**, 174–186 (2018). <https://doi.org/10.1016/j.enconman.2018.04.015>
4. A. Borisova, D. Popov, An option for the integration of solar photovoltaics into small nuclear power plant with thermal energy storage. *Sust. Energy Tech. Assess.* **18**, 119–126 (2016). <https://doi.org/10.1016/j.seta.2016.10.002>
5. R. Testoni, A. Bersano, S. Segantin, Review of nuclear microreactors: status, potentialities and challenges. *Prog. Nucl. Energ.* **138**, 103822 (2021). <https://doi.org/10.1016/j.pnucene.2021.103822>
6. C.J. Hu, D.L. Yu, M.S. He et al., Performance evaluation of ultra-long lithium heat pipe using an improved lumped parameter model. *Nucl. Sci. Tech.* **32**, 141 (2021). <https://doi.org/10.1007/s41365-021-00980-1>
7. W. Xiao, X. Li, P. Li et al., High-fidelity multi-physics coupling study on advanced heat pipe reactor. *Comput. Phys. Commun.* **270**, 108152 (2022). <https://doi.org/10.1016/j.cpc.2021.108152>
8. Y. Ma, W. Han, B. Xie et al., Coupled neutronic, thermal-mechanical and heat pipe analysis of a heat pipe cooled reactor. *Nucl. Eng. Des.* **384**, 111473 (2021). <https://doi.org/10.1016/j.nucengdes.2021.111473>
9. H. Cao, G. Wang, The research on the heat transfer of a solid-core nuclear reactor cooled by heat pipe through a numerical simulation, considering the assembly gaps. *Ann. Nucl. Energ.* **130**, 431–439 (2019). <https://doi.org/10.1016/j.anucene.2019.03.013>
10. B.T. Pham, J.J. Einerson, G.L. Hawkes et al., Impact of gap size uncertainty on calculated temperature uncertainty for the advanced gas reactor experiments. *Nucl. Eng. Des.* **329**, 110–123 (2018). <https://doi.org/10.1016/j.nucengdes.2017.08.009>
11. M. Wang, Y. Wang, W. Tian et al., Recent progress of CFD applications in PWR thermal hydraulics study and future directions. *Ann. Nucl. Energ.* **150**, 107836 (2021). <https://doi.org/10.1016/j.anucene.2020.107836>
12. D.H. Daher, M. Kotb, A.M. Khalaf et al., Simulation of a molten salt fast reactor using the COMSOL Multiphysics software. *Nucl. Sci. Tech.* **31**, 115 (2020). <https://doi.org/10.1007/s41365-020-00833-3>
13. B. Deng, Y. Cui, J.G. Chen et al., Core and blanket thermal–hydraulic analysis of a molten salt fast reactor based on coupling of OpenMC and OpenFOAM. *Nucl. Sci. Tech.* **31**, 85 (2020). <https://doi.org/10.1007/s41365-020-00803-9>
14. Y.L. Zhu, X.W. Chen, C. Hao et al., Implementation of high-fidelity neutronics and thermal–hydraulic coupling calculations in HNET. *Nucl. Sci. Tech.* **33**, 146 (2022). <https://doi.org/10.1007/s41365-022-01120-z>
15. I. Khan, M. Wang, Y. Zhang et al., Two-phase bubbly flow simulation using CFD method: a review of models for interfacial forces. *Prog. Nucl. Energ.* **125**, 103360 (2020). <https://doi.org/10.1016/j.pnucene.2020.103360>
16. T.Z. Bai, C.H. Peng, Thermal hydraulic characteristics of helical coil once-through steam generator under ocean conditions. *Nucl. Sci. Tech.* **33**, 134 (2022). <https://doi.org/10.1007/s41365-022-01108-9>
17. Z. Han, J. Zhang, M. Wang et al., A modified system analysis code for thermo-hydraulic calculation of hydrogen in a nuclear thermal propulsion (NTP) system. *Ann. Nucl. Energ.* **164**, 108632 (2021). <https://doi.org/10.1016/j.anucene.2021.108632>

18. C.L. Wang, T.C. Liu, S.M. Tang et al., Thermal–hydraulic analysis of space nuclear reactor TOPAZ-II with modified RELAP5. *Nucl. Sci. Tech.* **30**, 12 (2019). <https://doi.org/10.1007/s41365-018-0537-3>
19. J. Wang, Q. Wang, M. Ding, Review on neutronic/thermal-hydraulic coupling simulation methods for nuclear reactor analysis. *Ann. Nucl. Energ.* **137**, 107165 (2020). <https://doi.org/10.1016/j.anucene.2019.107165>
20. L. Ye, M. Wang, X. Wang et al., Thermal hydraulic and neutronics coupling analysis for plate type fuel in nuclear reactor core. *Sci. Tech. Nucl. Install.* **2020**, 2562747 (2020). <https://doi.org/10.1155/2020/2562747>
21. W.G. Li, C. Chang, Y. Qin et al., GPU-based cross-platform Monte Carlo proton dose calculation engine in the framework of Taichi. *Nucl. Sci. Tech.* **34**, 77 (2023). <https://doi.org/10.1007/s41365-023-01218-y>
22. S. Choi, W. Kim, J. Choe et al., Development of high-fidelity neutron transport code STREAM. *Comput. Phys. Commun.* **264**, 107915 (2021). <https://doi.org/10.1016/j.cpc.2021.107915>
23. Z.G. Li, K. Wang, Y.C. Guo et al., Forced propagation method for Monte Carlo fission source convergence acceleration in the RMC. *Nucl. Sci. Tech.* **32**, 27 (2021). <https://doi.org/10.1007/s41365-021-00868-0>
24. M.S. El-Genk, L. Huang, An experimental investigation of the transient response of a water heat pipe. *Int. J. Heat Mass Transf.* **36**, 1–3 (1993). [https://doi.org/10.1016/0017-9310\(93\)90062-B](https://doi.org/10.1016/0017-9310(93)90062-B)
25. Y. Ma, H. Yu, S. Huang et al., Effect of inclination angle on the startup of a frozen sodium heat pipe. *Appl. Therm. Eng.* **201**, 117625 (2022). <https://doi.org/10.1016/j.applthermaleng.2021.117625>
26. C. Wang, L. Zhang, X. Liu et al., Experimental study on startup performance of high temperature potassium heat pipe at different inclination angles and input powers for nuclear reactor application. *Ann. Nucl. Energ.* **136**, 107051 (2020). <https://doi.org/10.1016/j.anucene.2019.107051>
27. W. Teng, X. Wang, Y. Zhu, Experimental investigations on startup and thermal performance of sodium heat pipe under swing conditions. *Int. J. Heat Mass Transf.* **152**, 119505 (2020). <https://doi.org/10.1016/j.ijheatmasstransfer.2020.119505>
28. Y.C. Guo, Z.L. Su, Z.G. Li et al., Numerical investigation on the startup performance of high-temperature heat pipes for heat pipe cooled reactor application. *Nucl. Sci. Tech.* **32**, 104 (2021). <https://doi.org/10.1007/s41365-021-00947-2>
29. C. Wang, X. Liu, M. Liu et al., Experimental study on heat transfer limit of high temperature potassium heat pipe for advanced reactors. *Ann. Nucl. Energ.* **151**, 107935 (2021). <https://doi.org/10.1016/j.anucene.2020.107935>
30. D.I. Poston, P.R. McClure, D.D. Dixon et al., Experimental demonstration of a heat pipe–Stirling engine nuclear reactor. *Nucl. Technol.* **188**, 229–237 (2014). <https://doi.org/10.13182/NT13-71>
31. M. Lin, J. Mou, C. Chi et al., A space power system of free piston Stirling generator based on potassium heat pipe. *Front. Energ.* **14**, 1–10 (2020). <https://doi.org/10.1007/s11708-019-0655-6>
32. C. Wang, S. Tang, X. Liu et al., Experimental study on heat pipe thermoelectric generator for industrial high temperature waste heat recovery. *Appl. Therm. Eng.* **175**, 115299 (2020). <https://doi.org/10.1016/j.applthermaleng.2020.115299>
33. G.L. Hawkes, *Thermal Model Details and Description of the AGR-5/6/7 Experiment*. Tech. Rep., Idaho National Laboratory (2019). <https://www.osti.gov/servlets/purl/1599861>
34. Y. Guo, Z. Li, S. Huang et al., A new neutronics-thermal-mechanics multi-physics coupling method for heat pipe cooled reactor based on RMC and OpenFOAM. *Prog. Nucl. Energ.* **139**, 103842 (2021). <https://doi.org/10.1016/j.pnucene.2021.103842>
35. J.W. Sterbentz, J.E. Werner, M.G. Mckellar et al., *Special Purpose Nuclear Reactor (5 MW) for Reliable Power at Remote Sites Assessment Report*. Tech. Rep., Idaho National Laboratory (2017). <https://doi.org/10.2172/1410224>
36. S.K. Raju, G.N. Pillai, Design and real time implementation of type-2 fuzzy vector control for DFIG based wind generators. *Renew. Energ.* **88**, 40–50 (2016). <https://doi.org/10.1016/j.renene.2015.11.006>
37. P. Haase, B. Thomas, Test and optimization of a control algorithm for demand-oriented operation of CHP units using hardware-in-the-loop. *Appl. Energ.* **294**, 116974 (2021). <https://doi.org/10.1016/j.apenergy.2021.116974>
38. S. Quan, Y.X. Wang, X. Xiao et al., Disturbance prediction-based enhanced stochastic model predictive control for hydrogen supply and circulating of vehicular fuel cells. *Energ. Convers. Manag.* **238**, 114167 (2021). <https://doi.org/10.1016/j.enconman.2021.114167>
39. H. He, R. Xiong, K. Zhao et al., Energy management strategy research on a hybrid power system by hardware-in-loop experiments. *Appl. Energ.* **112**, 1311–1317 (2013). <https://doi.org/10.1016/j.apenergy.2012.12.029>
40. M.O. Faruque, T. Strasser, G. Lauss et al., Real-time simulation technologies for power systems design, testing, and analysis. *IEEE Pow. Energ. Tech. Syst. J.* **2**, 63–73 (2015). <https://doi.org/10.1109/JPEETS.2015.2427370>
41. W. Guo, Y. Li, Y.Z. Li et al., An integrated hardware-in-the-loop verification approach for dual heat sink systems of aerospace single phase mechanically pumped fluid loop. *Appl. Therm. Eng.* **106**, 1403–1414 (2016). <https://doi.org/10.1016/j.applthermaleng.2016.06.140>
42. J. Bélanger, P. Venne, *The What, Where and Why of Real-Time Simulation*. Tech. Rep., OPAL-RT Technol (2010). https://blobt.estweb.opal-rt.com/medias/L00161_0436.pdf
43. P.R. McClure, D.I. Poston, V. Dasari et al., *Design of Megawatt Power Level Heat Pipe Reactors*. Tech. Rep., Los Alamos National Laboratory (2015). <https://doi.org/10.2172/1226133>
44. Z. Duan, J. Zhang, Y. Wu et al., Multi-physics coupling analysis on neutronics, thermal hydraulic and mechanics characteristics of a nuclear thermal propulsion reactor. *Nucl. Eng. Des.* **399**, 112042 (2022). <https://doi.org/10.1016/j.nucengdes.2022.112042>
45. P.K. Romano, B. Forget, The OpenMC Monte Carlo particle transport code. *Ann. Nucl. Energ.* **51**, 274–281 (2013). <https://doi.org/10.1016/j.anucene.2012.06.040>
46. H. Guo, K.Y. Feng, H.Y. Gu et al., Neutronic modeling of megawatt-class heat pipe reactors. *Ann. Nucl. Energ.* **154**, 108140 (2021). <https://doi.org/10.1016/j.anucene.2021.108140>
47. H.X. Chen, Y.X. Guo, D.Z. Yuan et al., Experimental study on frozen startup and heat transfer characteristics of a cesium heat pipe under horizontal state. *Int. J. Heat Mass Transf.* **183**, 122105 (2022). <https://doi.org/10.1016/j.ijheatmasstransfer.2021.122105>
48. S.M. Yang, Z.Z. Zhang, An experimental study of natural convection heat transfer from a horizontal cylinder in high Rayleigh number laminar and turbulent regions. In *Proceedings of the 10th International Heat Transfer Conference* (Brighton, 1994)
49. M. Zarei, A physically based PID controller for the power maneuvering of nuclear reactors. *Prog. Nucl. Energ.* **127**, 103431 (2020). <https://doi.org/10.1016/j.pnucene.2020.103431>
50. C. Elliott, V. Vijayakumar, W. Zink et al., National instruments LabVIEW: a programming environment for laboratory. *J. Assoc. Lab. Autom.* **12**, 17–24 (2007). <https://doi.org/10.1016/j.jala.2006.07.012>
51. S.M. Bragg-Sitton, J.P. Holloway, Autonomous reactor control using model based predictive control for space propulsion

- applications. *Ann. Nucl. Energy* **33**, 1368–1378 (2006). <https://doi.org/10.1016/j.anucene.2006.09.007>
52. M. Mahdavi, S. Tiari, S. Qiu, Experimental study of the thermal characteristics of a heat pipe. *Exp. Therm. Fluid. Sci.* **93**, 292–304 (2018). <https://doi.org/10.1016/j.expthermflusci.2018.01.003>
53. S.M. Bragg-Sitton, T.J. Godfroy, K. Webster, Improving the fidelity of electrically heated nuclear systems testing using simulated neutronic feedback. *Nucl. Eng. Des.* **240**, 2745–2754 (2010). <https://doi.org/10.1016/j.nucengdes.2010.04.036>

Springer Nature or its licensor (e.g. a society or other partner) holds exclusive rights to this article under a publishing agreement with the author(s) or other rightsholder(s); author self-archiving of the accepted manuscript version of this article is solely governed by the terms of such publishing agreement and applicable law.